Chapter 7
Dislocation Microstructure

One of the most profound consequences of irradiation on the microstructure of materials is the formation of dislocation loops. Dislocation loops have a bias for interstitials and thus have a strong impact on the development of the irradiated microstructure. They also influence the deformation behavior and, consequently, the ductility and hardening of irradiated materials, as will be discussed in Chap. 12. In this chapter, we will review the origin and character of dislocations, their mobility and multiplication and their stresses, strains and energies. The character of dislocation loops will be examined, and models for nucleation and growth will be presented. Finally, the stacking fault tetrahedron (SFT) will be discussed. For a more in-depth treatment of dislocations, the reader is referred to [1–4].

7.1 Dislocation Lines

The discovery of dislocations in crystals has its origin in the discrepancy between the measured and theoretical stress needed to cause shear in a crystal. Consider the stress required to shear a crystal along a given atomic plane. A shear of one atomic distance requires that atoms above the plane all move one lattice spacing relative to those below (Fig. 7.1). To reach the saddle point, each atom must move horizontally a distance of one atom radius, a. Since the separation of two planes is $\sim 2a$, the shear strain at the saddle point is $\gamma \approx a/2a \sim 1/2$. In a perfectly elastic crystal, the ratio of shear stress to shear strain is the shear modulus:

$$\frac{\sigma_s}{\gamma} = \mu. \qquad (7.1)$$

For a typical shear modulus of 17 GPa and a shear strain of 1/2, the shear stress from Eq. (7.1) is ~ 8.5 GPa. However, experiments, for example on magnesium, produce deformation at shear stresses of ~ 1 MPa, which is different from theory by
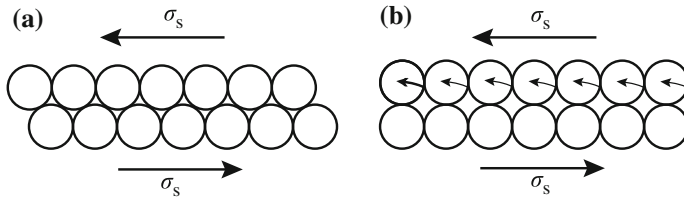
Fig. 7.1 Initial position of atoms above and below a slip plane and the motion of the atoms above the slip plane required to cause slip
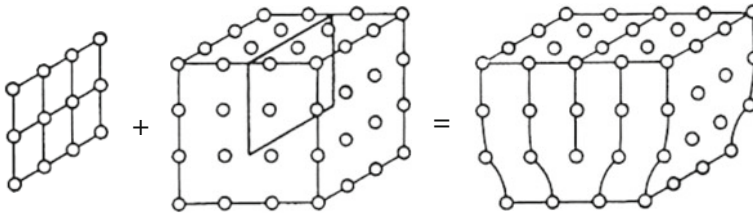
Fig. 7.2 An edge dislocation described as an extra half plane of atoms above the slip plane

a factor of 10^4! The reason is the existence of dislocations that provide for much reduced shear stresses in crystals.

A *dislocation* is a line that forms a boundary between a region of the crystal that has slipped and one that has not. The two basic types of dislocations lines are the edge and the screw. In an *edge dislocation*, atoms over the cut surface are shifted in a direction *perpendicular* to the dislocation line. An edge dislocation can also be thought of as the insertion of an extra half plane of atoms (Fig. 7.2). In a *screw dislocation*, the atoms over the cut surface are shifted in a direction *parallel* to the dislocation line (Fig. 7.3a). The screw dislocation itself is a pole about which a spiral ramp of planes circles (analogous to a parking garage ramp) (Fig. 7.3b). There also exist *mixed dislocations* in which the shift is neither parallel nor perpendicular to the dislocation line, but at some arbitrary angle. Figure 7.4 shows a mixed dislocation in a crystal in which the dislocation line is curved. Note that the boundary separating slipped and unslipped regions is circular. At point A (front face), the dislocation is of pure edge character. At point B (side face), the dislocation is of pure screw character. In between, the dislocation is *mixed* with the proportion of screw character and edge character varying continuously with distance along the line. Figure 7.5 shows the construction of a mixed dislocation.

A dislocation line can also be made in the form of a closed loop rather than a line that terminates at the crystal surface. Following Fig. 7.6, we make a cut along ABCD and shift the atoms parallel to the plane and then rejoin them. Note that segments AB and DC have edge character and segments BC and AD have screw character. Segments AB and DC have opposite sign in that one has a half plane above the cut and one has the half plane below it. The same is true with segments BC and AD. This loop is termed a *perfect* dislocation loop.
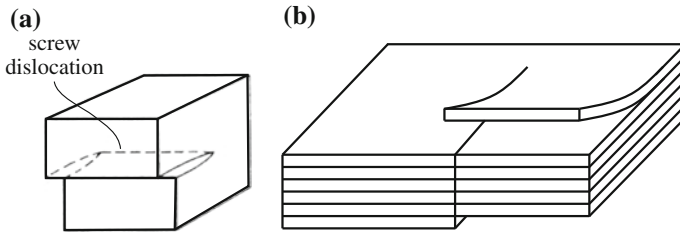
Fig. 7.3 (**a**) A screw dislocation formed by a cut and a shift of atoms in a direction parallel to the *cut line*. (**b**) A schematic showing the "parking ramp" nature of a screw dislocation in which atom planes spiral about the dislocation line
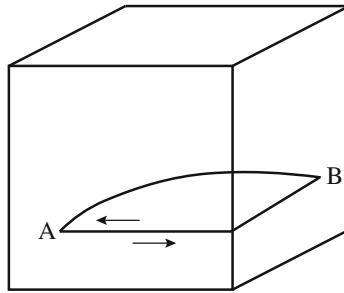
Fig. 7.4 Curved dislocation line with pure edge character at point *A*, pure screw character at point *B*, and mixed character along the length of the dislocation

Now suppose that instead of shifting atoms parallel to the plane as we did in the example of a perfect loop, we fill up the cut with more atoms. The shift of atoms on each side of the cut is *perpendicular* to the surface. Figure 7.7 shows that by insertion of a disk of atoms into the cut, that every segment of the dislocation loop has pure edge character. This is very different from the perfect loop with edge character and screw character. This dislocation loop is called a *prismatic* or *Frank* loop. One variation is to remove a disk of atoms from the cut rather than insert an extra plane of atoms.

7.1.1 Dislocation Motion

Dislocations can move in two modes: glide and climb. Glide is the motion of a dislocation on its slip plane and is a conservative motion in that it requires no long-range mass transport in order to occur. Experiments have shown that the logarithm of the dislocation velocity is proportional to the logarithm of the shear stress causing glide:
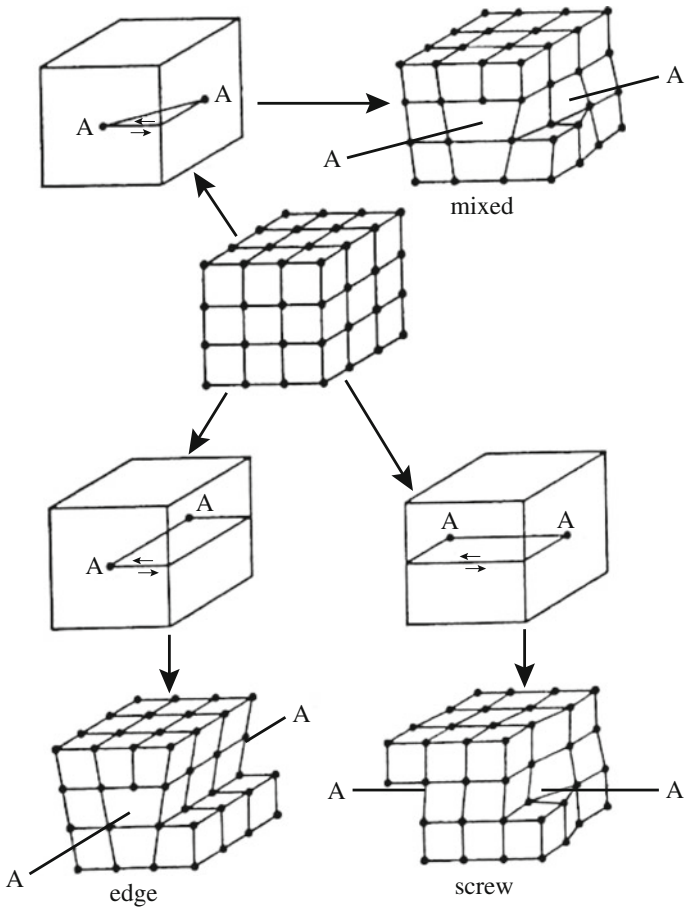
Fig. 7.5 Construction of a dislocation line with mixed character
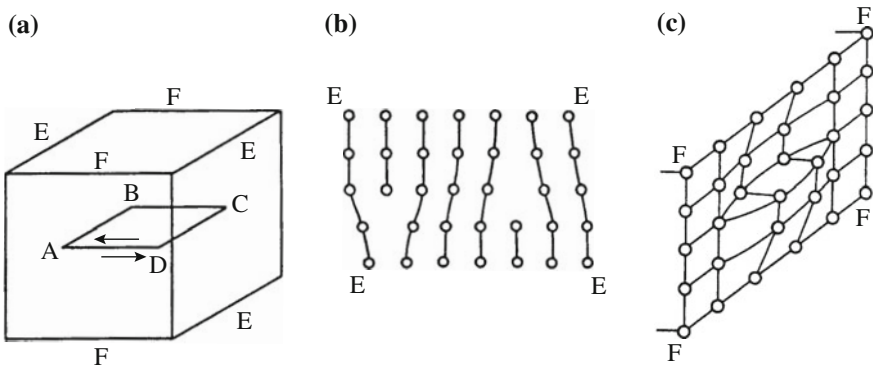
Fig. 7.6 A perfect dislocation loop in a crystal in which the character of the loop varies with position along the loop

Fig. 7.7 A Frank dislocation loop formed by insertion of a circular plane of atoms between existing planes in the lattice
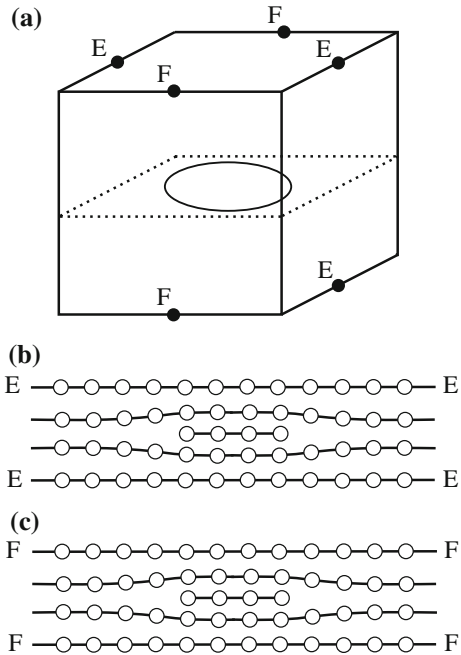
$$\ln v_g \propto \ln \sigma_s, \tag{7.2}$$

which implies a power law relationship between shear stress and dislocation velocity:

$$v_g = \left(\frac{\sigma_s}{\sigma_D}\right)^m, \tag{7.3}$$

where m is the stress exponent (~ 1.65), and σ_D is the value of the stress that yields a dislocation velocity of 0.01 m/s [5]. Experiments also show that the logarithm of the dislocation velocity is proportional to the reciprocal of the absolute temperature, T:

$$\ln v_g \propto \frac{1}{T}, \tag{7.4}$$

leading to the following description of the velocity of a gliding dislocation in terms of stress and temperature:

$$v_g = f(\sigma)\exp(-E/kT). \tag{7.5}$$

When dislocations glide, they displace the crystal above the slip plane relative to that below. Figure 7.8 shows that if an edge dislocation glides to the surface, the
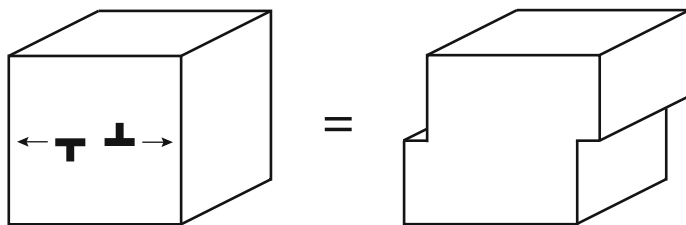
Fig. 7.8 Slip produced by movement of edge dislocations to the surface of a crystal
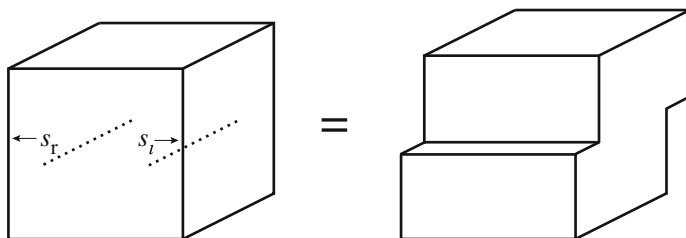
Fig. 7.9 Slip produced by movement of screw dislocations to the surface of a crystal

result is a step on the surface of magnitude equal to the Burgers vector. Screw dislocations will also produce a step on the surface, but on a face that is perpendicular to the dislocation line (Fig. 7.9). The perfect loop described in the last section will also result in displacement of the crystal when it reaches the surface. Figure 7.10 shows the displacement of the crystal above the slip plane relative to that below. Note that the displacements are entirely consistent with the character of the dislocation where it intersects the surface as shown in Figs. 7.8 and 7.9.

A Frank loop is essentially an edge dislocation. The slip plane for this type of loop is defined by the intersection of the loop edge and the adjacent crystal and consists of a cylindrical surface projecting above and below the plane of the loop. Figure 7.11 shows how surface atoms would be displaced if the loop was to glide to the surface. However, this mode of motion is not energetically favorable, and this loop is more likely to move by climb rather than glide.

Dislocations also move by a non-conservative process called *climb*. Climb is an important process for edge dislocations and prismatic loops, since unlike screw dislocations that can glide on *any* plane containing the dislocation, there is only one possible slip plane for an edge dislocation to glide. Climb is the extension or recession of the extra half plane of atoms by absorption or emission of a vacancy, absorption of an interstitial atom, or emission/absorption of clusters of vacancies or single interstitial atoms (SIAs). Figure 7.12 shows the positive climb of an edge dislocation by absorption of a vacancy at the dislocation core. In order for the edge dislocation to move up one lattice spacing, all of the atoms along the edge (into the paper) must absorb a vacancy. Positive climb results in a decrease in the size of the extra half plane, while negative climb results in the increase in the size of the extra
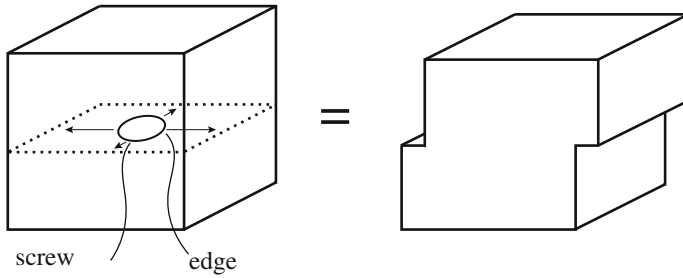
Fig. 7.10 Slip produced by movement of a perfect dislocation loop to the surface of a crystal
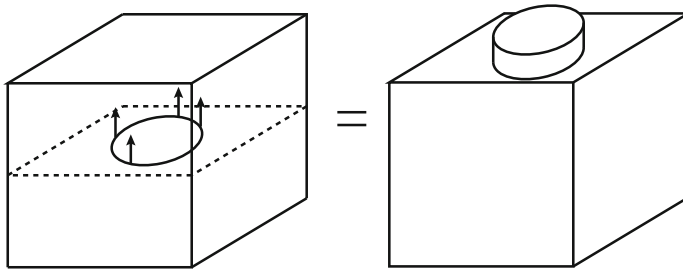
Fig. 7.11 Slip produced by movement of a Frank loop to the surface of a crystal
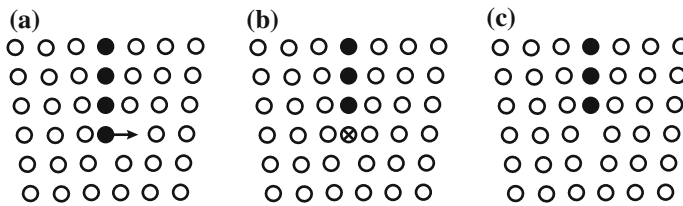
Fig. 7.12 Positive climb of an edge dislocation by absorption of vacancies at its core

half plane. Positive climb is associated with a compressive strain and will be promoted by a compressive stress component perpendicular to the extra plane. Similarly, a tensile stress applied perpendicular to the extra plane promotes growth of the plane and thus negative climb. Since they are essentially edge dislocations, Frank loops climb in the same manner, where positive climb results in loop shrinkage and negative climb results in loop growth. Note that there is a fundamental difference between the nature of the stress that produces slip and that which produces climb. Slip occurs as the result of shear stress, and climb occurs as a result of a normal stress.

Since climb requires that vacancies move through the lattice either to or away from the extra half plane, the rate of climb will be dependent on both the diffusion

coefficient of vacancies and their concentration. In unirradiated solids, this means that climb will be most important at high temperature. However, in irradiated solids, the increased population of vacancies will make climb more important at lower temperatures. Further, the elevated concentration of interstitials means that they too can contribute to climb in a direction that is opposite to that of vacancies.

7.1.2 Description of a Dislocation

A description of a dislocation consists of the specification of the vector defining the line direction, s, and the Burgers vector defining the atom shift, b. The Burgers vector is defined as follows:

1. Define a positive direction, s, along the dislocation line (e.g., into the paper).
2. Construct a plane perpendicular to the dislocation line.
3. Starting in a region of perfect crystal (away from the dislocation core), complete a counterclockwise circuit around the dislocation line (in the plane of the paper)
4. The Burgers vector, b, is the vector needed to close the circuit.

The rule is shown schematically in Fig. 7.13 for a screw dislocation. Following this convention, the Burgers vector of an edge dislocation is *perpendicular* to the dislocation line. The Burgers vector of a screw dislocation is *parallel* to the dislocation line.

For an edge dislocation, we can determine the Burgers vector in the following manner. Sighting down the dislocation line (along the positive s direction), we make a counterclockwise circuit around the dislocation. The vector connecting the end point to the origin is the Burgers vector. Figure 7.14 shows an example of the determination of the Burgers vector using the construction rule. (Note that it does not matter which direction is called positive, but we need to adopt a convention in order to determine the orientation of the line and the extra half plane in the crystal. If we sighted in the opposite direction, b will be in the opposite direction. What matters is the specification of s *relative to* b.) Following the convention, Fig. 7.15a shows a dislocation with line direction, s, pointing into the paper and b pointing to the left. The dislocation in Fig. 7.15b is identical to that in Fig. 7.15a since the
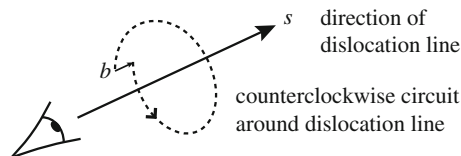
Fig. 7.13 Convention for finding the Burgers vector of a dislocation line characterized by direction s
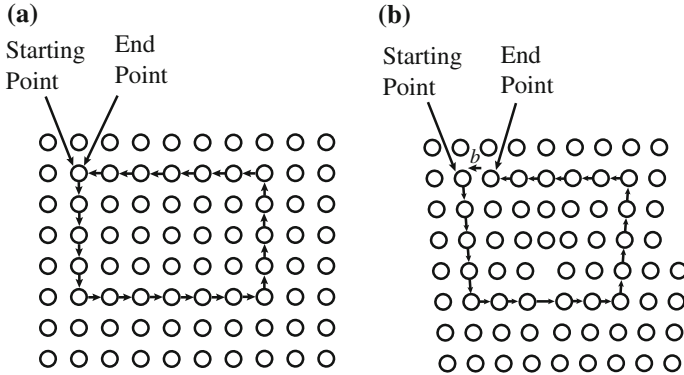
Fig. 7.14 The Burgers circuit for an edge dislocation following the convention shown in Fig. 7.13 for (**a**) a region of perfect crystal, and (**b**) a region containing an edge dislocation
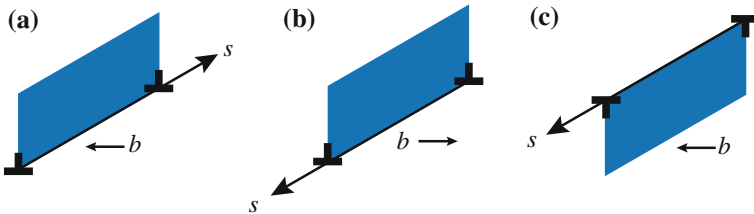
Fig. 7.15 Examples of identical edge dislocations (**a**) and (**b**) and an edge dislocation of opposite sign (**c**)

relationship between *s* and *b* is the same. However, the dislocation shown in Fig. 7.15c is of opposite sign.

For a screw dislocation, we consider a left-handed screw (counterclockwise rotation; see Fig. 7.16). With this convention, *s* and *b* are in the same direction. Figure 7.17a shows a screw dislocation with Burgers vector in the same direction as *s*. The dislocation shown in Fig. 7.17b is identical to that in Fig. 7.17a, but the dislocation shown in Fig. 7.17c is of opposite sign as the other two.

An edge dislocation glides in the direction of its Burgers vector. A screw dislocation glides in a direction *perpendicular to* its Burgers vector. We adopt the following convention to determine the direction of motion of a dislocation line. *The positive direction of motion is obtained by a counterclockwise rotation on a plane parallel to the slip plane and through* 90° *from the positive direction of the dislocation line itself.* The rule is shown by the illustration in Fig. 7.18a. Figure 7.18b, c shows the positive direction of motion for an edge and screw dislocation, respectively. Figure 7.19 shows the direction of motion for a dislocation loop that is characterized by a single Burgers vector (perfect loop) and changes character along the dislocation line.
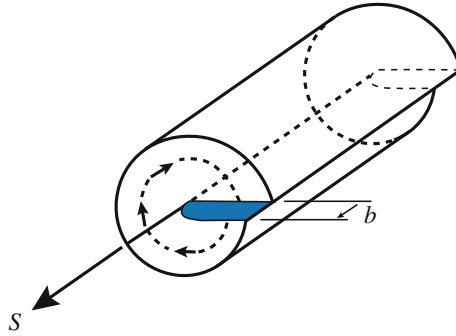
Fig. 7.16 The Burgers circuit for a screw dislocation following the convention shown in Fig. 7.13
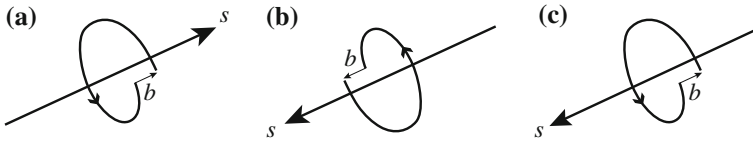
Fig. 7.17 Examples of identical screw dislocations (**a**) and (**b**), and a screw dislocation of opposite sign (**c**)

7.1.3   Displacements, Strains, and Stresses

Dislocations interact with each other and with other microstructure features through their stress fields. Therefore, it is important to establish the stress and strain fields around a dislocation as well as the energy associated with the dislocation line. We will begin with the screw dislocation and then treat the edge dislocation. Recall the orientation of the screw dislocation is one in which the Burgers vector is parallel to the dislocation line, which means that the displacement of atoms is in the direction of the dislocation line. If we describe the dislocation in cylindrical coordinates, Fig. 7.20, then there is no displacement along the r or θ directions so that:

$$u_r = u_\theta = 0. \tag{7.6}$$

In Cartesian coordinates, the displacement in the x–y plane is zero. The only displacement is in the z-direction, and from inspection, we have in cylindrical coordinates:

$$u_z = \frac{b}{2\pi}\theta, \quad u_x = u_y = 0, \tag{7.7}$$
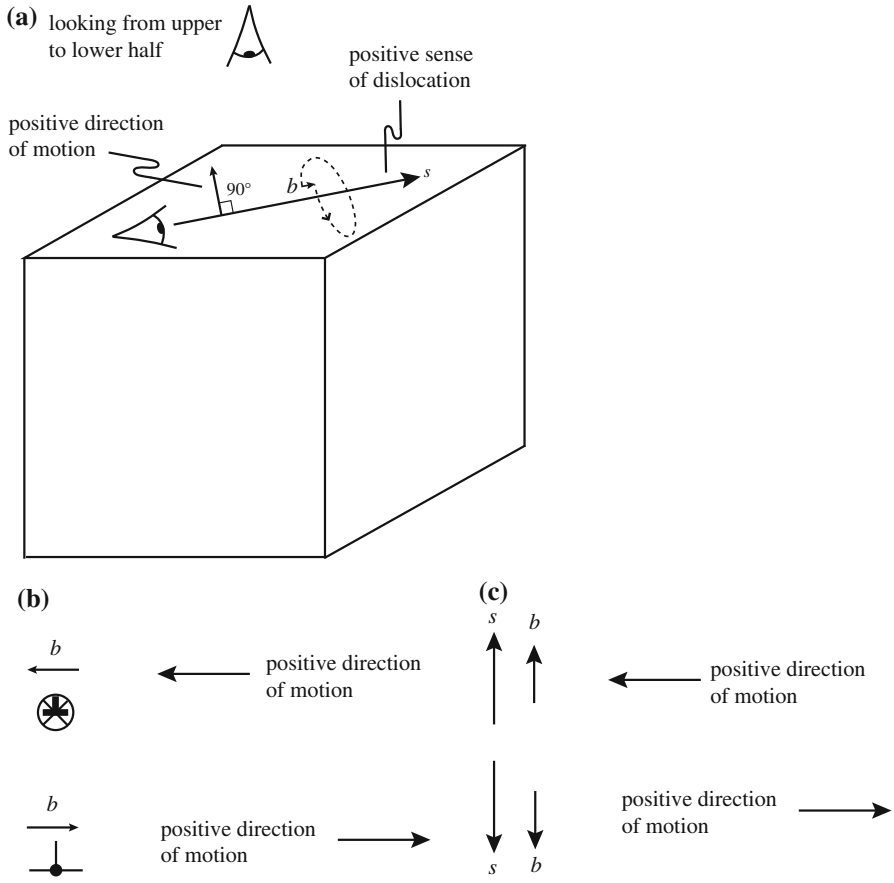
Fig. 7.18 (**a**) Rule for determination of the direction of motion of a dislocation on its slip plane and examples of the positive direction of motion for (**b**) edge and (**c**) screw dislocations
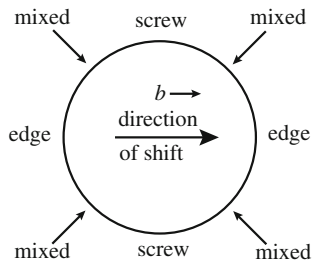
Fig. 7.19 Positive direction of motion of a perfect loop characterized by a single Burgers vector

Fig. 7.20 Screw dislocation
in the Cartesian coordinate
system
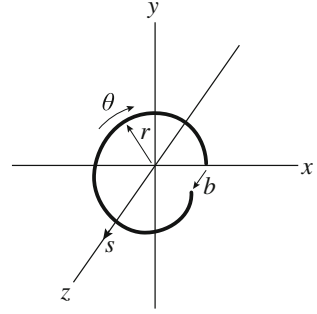
and in Cartesian coordinates:

$$u_z = \frac{b}{2\pi} \tan^{-1} \frac{y}{x},\tag{7.8}$$

where b is the magnitude of the Burgers vector. From elasticity theory, we can
calculate the strain from the displacement as:

$$\varepsilon_{\theta z} = \frac{1}{r}\left(\frac{\partial u_z}{\partial \theta}\right) = \frac{b}{2\pi r}, \quad \varepsilon_{rr} = \varepsilon_{\theta\theta} = \varepsilon_{zz} = \varepsilon_{r\theta} = \varepsilon_{rz} = 0,\tag{7.9}$$

and in Cartesian coordinates:

$$\begin{aligned}
\varepsilon_{xz} &= \frac{b}{2\pi}\frac{y}{x^2+y^2} = \frac{b}{2\pi r}\sin\theta \\
\varepsilon_{yz} &= -\frac{b}{2\pi}\frac{x}{x^2+y^2} = -\frac{b}{2\pi r}\cos\theta \\
\varepsilon_{xx} &= \varepsilon_{yy} = \varepsilon_{zz} = \varepsilon_{xy} = 0.
\end{aligned}\tag{7.10}$$

The stress field of the screw dislocation is determined from the relation between
stress and strain:

$$\sigma_{\theta z} = \mu\varepsilon_{\theta z} = \frac{\mu b}{2\pi r}, \quad \sigma_{rr} = \sigma_{\theta\theta} = \sigma_{zz} = \sigma_{r\theta} = \sigma_{rz} = 0,\tag{7.11}$$

and

$$\begin{aligned}
\sigma_{xz} &= \frac{\mu b}{2\pi}\frac{y}{x^2+y^2} = \frac{\mu b}{2\pi r}\sin\theta \\
\sigma_{yz} &= -\frac{\mu b}{2\pi}\frac{x}{x^2+y^2} = -\frac{\mu b}{2\pi r}\cos\theta \\
\sigma_{xx} &= \sigma_{yy} = \sigma_{zz} = \sigma_{xy} = 0.
\end{aligned}\tag{7.12}$$

Fig. 7.21 Edge dislocation in the Cartesian coordinate system
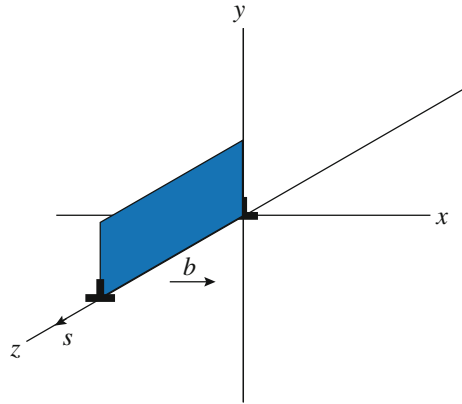
For an edge dislocation as shown in Fig. 7.21, the displacement of atoms is in the x-direction. The displacement is not so simple here, but we know that the dislocation will be similar at any point along the z-axis and hence, the stress state is one of plane stress. The displacement field around the edge dislocation in Cartesian coordinates is:

$$u_x = \frac{b}{2\pi}\left[\tan^{-1}\frac{y}{x} + \frac{\lambda+u}{\lambda+2\mu}\frac{xy}{x^2+y^2}\right]$$

$$u_y = \frac{b}{2\pi}\left[\frac{-\mu}{2(\lambda+2\mu)}\log\frac{x^2+y^2}{c} + \frac{\lambda+\mu}{\lambda+2\mu}\frac{y^2}{x^2+y^2}\right] \qquad (7.13)$$

$$u_z = 0,$$

where the constant c is added to make the log term dimensionless, but is irrelevant since stresses and strains are derivatives of the displacements. The resulting strains are as follows:

$$\varepsilon_{xx} = -\frac{by}{2\pi}\frac{\mu y^2 + (2\lambda+3\mu)x^2}{(\lambda+2\mu)(x^2+y^2)^2}$$

$$\varepsilon_{yy} = \frac{by}{2\pi}\frac{(2\lambda+\mu)x^2 - \mu y^2}{(\lambda+2\mu)(x^2+y^2)^2} \qquad (7.14)$$

$$\varepsilon_{xy} = \frac{b}{2\pi(1-v)}\frac{x(x^2-y^2)}{(x^2+y^2)^2}$$

$$\varepsilon_{zz} = \varepsilon_{xz} = \varepsilon_{yz} = 0,$$

where v is Poisson's ratio, λ is the Lamé constant, and $v = \frac{\lambda}{2(\lambda+\mu)}$. The stresses around an edge dislocation are then:

$$\sigma_{xx} = \frac{-\mu b}{2\pi(1-v)}\frac{y(3x^2+y^2)}{(x^2+y^2)^2} = \frac{-\mu b}{2\pi(1-v)r}\sin\theta(2+\cos 2\theta)$$

$$\sigma_{yy} = \frac{\mu b}{2\pi(1-v)}\frac{y(x^2-y^2)}{(x^2+y^2)^2} = \frac{\mu b}{2\pi(1-v)r}\sin\theta\cos 2\theta$$

$$\sigma_{xy} = -\frac{\mu b}{2\pi(1-v)}\frac{x(x^2-y^2)}{(x^2+y^2)^2} = \frac{\mu b}{2\pi(1-v)r}\cos\theta\cos 2\theta \qquad (7.15)$$

$$\sigma_{zz} = v(\sigma_{xx}+\sigma_{yy}) = \frac{-\mu vby}{\pi(1-v)(x^2+y^2)} = \frac{-\mu vb}{\pi(1-v)r}\sin\theta$$

$$\sigma_{xz} = \sigma_{yz} = 0.$$

The stresses in cylindrical coordinates are as follows:

$$\sigma_{rr} = \sigma_{\theta\theta} = \frac{\mu b}{2\pi(1-v)}\frac{\sin\theta}{r}$$

$$\sigma_{r\theta} = \frac{-\mu b}{2\pi(1-v)}\frac{\cos\theta}{r}$$

$$\sigma_{zz} = \frac{-\mu vb}{2\pi(1-v)}\frac{\sin\theta}{r} \qquad (7.16)$$

$$\sigma_{\theta z} = \sigma_{rz} = 0.$$

7.1.4 Energy of a Dislocation

Energy is stored in any elastic medium that is stressed. Applying a tensile stress to a rod produces a tensile strain, which is proportional to the stress in an elastic solid. Consider a unit cube within the rod. A stress, σ, is the total force applied across a face of the cube. The strain is the fractional distance the cube elongates in the direction of the stress. So the work done (energy/unit volume) on the cube is the force times the distance, or:

$$W = \int_0^{\varepsilon_{max}} \sigma d\varepsilon, \qquad (7.17)$$

and from Fig. 7.22, we have:

$$W = 1/2\sigma_{max}\varepsilon_{max}. \qquad (7.18)$$

Fig. 7.22 Elastic stress–strain curve showing the stored energy in the strain field
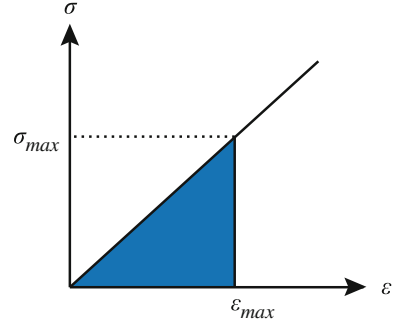
For a generalized stress field, the stored energy per unit volume is as follows:

$$W = 1/2\left(\sigma_{xx}\varepsilon_{xx} + \sigma_{yy}\varepsilon_{yy} + \sigma_{zz}\varepsilon_{zz} + \sigma_{xy}\varepsilon_{xy} + \sigma_{xz}\varepsilon_{xz} + \sigma_{yz}\varepsilon_{yz}\right), \tag{7.19}$$

and in cylindrical coordinates:

$$W = 1/2(\sigma_{rr}\varepsilon_{rr} + \sigma_{\theta\theta}\varepsilon_{\theta\theta} + \sigma_{zz}\varepsilon_{zz} + \sigma_{r\theta}\varepsilon_{r\theta} + \sigma_{rz}\varepsilon_{rz} + \sigma_{\theta z}\varepsilon_{\theta z}), \tag{7.20}$$

where $\sigma_{ij} = \sigma_{ji}$.

Applying Eq. (7.20) to the screw dislocation gives:

$$W = 1/2(\sigma_{\theta z}\varepsilon_{\theta z}) = \frac{\mu b^2}{8\pi^2 r^2}. \tag{7.21}$$

The elastic energy per unit length of the dislocation line is:

$$E_l = \int_{r_c}^{R} W 2\pi r \mathrm{d}r = \frac{\mu b^2}{4\pi} \int_{r_c}^{R} \frac{\mathrm{d}r}{r} = \frac{\mu b^2}{4\pi} \ln\left(\frac{R}{r_c}\right) + \varepsilon_c. \tag{7.22}$$

The limits on the integral are the dislocation core radius, r_c, and R. The dislocation core radius is that distance below which linear elasticity does not hold and is generally taken to be several Burgers vectors in magnitude. R is the outer dimension of the crystal, or for polycrystalline materials, R could be taken to be the grain radius. However, a further constraining condition is the presence of other dislocations, which is the case even in a well-annealed metal in which the dislocation density is still $\sim 10^8$ cm^{-2}. So R is often taken to be the distance midway to the next dislocation. However, the elastic energy is not highly sensitive to R since it appears in the ln term. The term ε_c is the energy of the dislocation core radius, which is not included in the integral since linear continuum elasticity theory breaks down in this region. Assuming that the stress level in the core is $\mu/30$, then for a dislocation core radius of $5b$, the value of ε_c is approximately $\mu b^2/10$, which is about 10–20 % of the value of that in the elastic strain field (ln term).

For an edge dislocation, the elastic energy per unit length determined in the same way as for the screw dislocation is as follows:

$$E_l = \frac{\mu b^2}{4\pi(1 - v)} \ln\left(\frac{R}{r_c}\right) + \varepsilon_c, \tag{7.23}$$

which is different from the screw dislocation by a factor of $(1 - v)$ in the denominator of the first term, or a factor of about 1.6 for $v \sim 0\,3$. For typical values of R and r_c, $\frac{\mu b^2}{2} \le E_l \le \mu b^2$. The elastic energy per unit length of dislocation line is also called the line tension and is denoted by Γ. Generally, Γ is taken to have the value $\frac{\mu b^2}{2}$.

7.1.5 Line Tension of a Dislocation

Under a uniform applied shear stress, σ_s, an element of dislocation line, ds, is displaced in a direction normal to ds by an amount dl (Fig. 7.23). The area swept out by the dislocation line element, ds, is dsdl. The average displacement of the crystal above the slip plane relative to that below is by an element:

$$dx = \left(\frac{dsdl}{A}\right) b, \tag{7.24}$$

where A is the area of the slip plane. The force creating the shear stress is $\sigma_s A$, and the work done is as follows:

$$dW = Fdx = \sigma_s A\left(\frac{dsdl}{A}\right) b \tag{7.25}$$

$$= \sigma_s dsdlb.$$

Fig. 7.23 Dislocation line segment ds sweeping out an area dsdl in the direction of the Burgers vector
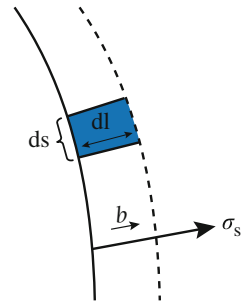
Since force is work divided by the distance over which it is applied:

$$F = \frac{dW}{dl} = \sigma_s ds b, \tag{7.26}$$

and the force per unit length is as follows:

$$F_l = \frac{dW/dl}{ds} = \sigma_s b. \tag{7.27}$$

Consider a curved dislocation line. The line tension produces an inward radial force that tends to straighten out the dislocation line. The dislocation will only remain curved if a shear stress exists to resist the line tension. We wish to determine the shear stress required to maintain the curvature. Consider a segment of a dislocation line as shown in Fig. 7.24. The outward force due to the shear stress is as follows:

$$\sigma_s b ds = 2\sigma_s b R d\theta. \tag{7.28}$$

The inward restraining force is as follows:

$$2\Gamma \sin(d\theta) \sim 2\Gamma d\theta. \tag{7.29}$$

From Eqs. (7.28) and (7.29), we have the force balance:

$$2\Gamma d\theta = 2\sigma_s b R d\theta, \tag{7.30}$$

and solving for σ_s yields the shear stress in terms of the line tension:

$$\sigma_s = \frac{\Gamma}{bR}. \tag{7.31}$$

For:

$$\Gamma \approx \frac{\mu b^2}{2}, \quad \text{then} \quad \sigma_s = \frac{\mu b}{2R}, \tag{7.32a}$$
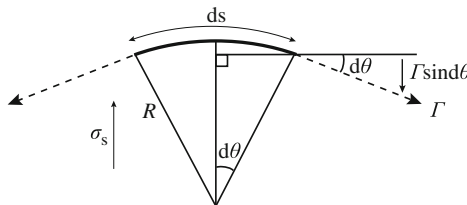
Fig. 7.24 Inward restraining force on a dislocation line segment ds due to a shear stress σ_s
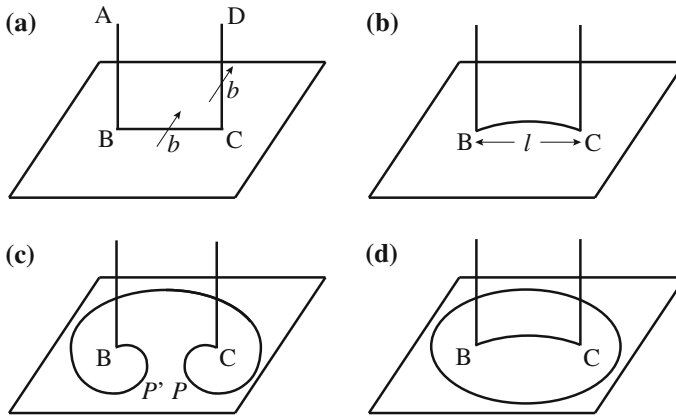
Fig. 7.25 Frank–Read source for the production of dislocations

and for

$$\Gamma \approx \mu b^2, \quad \text{then} \quad \sigma_s = \frac{\mu b}{R}. \tag{7.32b}$$

One mechanism of formation of dislocations in solids is the Frank–Read mechanism. The mechanism is shown in Fig. 7.25 and occurs as follows. A dislocation line segment defined by ABCD and Burgers vector b is such that segments AB and DC are immobile and only segment BC lies in a slip plane. The dislocation segment BC is pinned at the points B and C. The temperature is assumed to be low enough that that climb is not an option. Under an applied stress, the segment BC bows out slightly in response to the stress and adopts the curvature as prescribed by the line tension on the dislocation given in Eq. (7.32a) $\sigma_s = \frac{\mu b}{2R}$, and for $l = 2R$, $\sigma_s \approx \frac{\mu b}{l}$. When the force arising from the curvature of the dislocation line can no longer balance the force produced by the applied stress, the dislocation becomes unstable and bows out to adopt the configuration shown in Fig. 7.25c. Note that at this point, the line segments P and P' have opposite character, and as the dislocation continues to bow out, they come in contact with each other and annihilate, leaving a region of perfect crystal and a perfect loop. The applied shear stress will cause the loop to expand and will also start the process of creating a new loop from the same BC segment. This process can continue to occur, and one such pinned dislocation can produce many loops and will continue as long as the loops are able to expand away from the source. Figure 7.26 shows a micrograph of a Frank–Read source in a silicon crystal. Eventually, the back stress caused by the previous loops will produce a retarding force on the source, and it will shut down. Back stress due to dislocation pileup is discussed in Chap. 12.
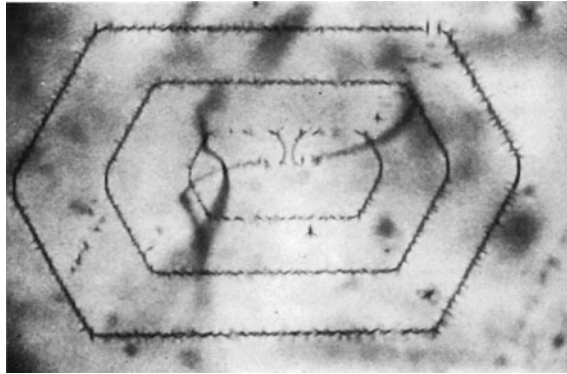
Fig. 7.26 Micrograph of a Frank–Read source in a silicon crystal (from [6])

7.1.6   Forces on a Dislocation

We consider here the application of an external stress on a solid containing a dislocation. For example, the application of a shear stress, σ_{xy}, on a solid containing an edge dislocation (Fig. 7.27) produces motion in the $+x$-direction. In moving a dislocation a distance L, the external applied stress will have done an amount of work/unit length of dislocation line equal to $\sigma_{xy}bL$. Then, the force is $F = \sigma_{xy}b$. Note that the force is in the $+x$-direction.

For a screw dislocation, application of a shear stress, σ_{yz}, results in a force $\sigma_{yz}b$, where the force is in the $+x$-direction (Fig. 7.28). Application of a shear stress σ_{xz} produces a force $-\sigma_{xz}b$, where the force is in the $-y$-direction, and motion is perpendicular to the slip plane.

What if we apply a stress to an edge dislocation that produces a force in a direction perpendicular to the slip plane? A tensile stress, σ_{xx}, applied to the edge dislocation in Fig. 7.29 will produce a downward force on the dislocation equal to $-\sigma_{xx}b$. The only way that the dislocation can respond to this stress is to climb.
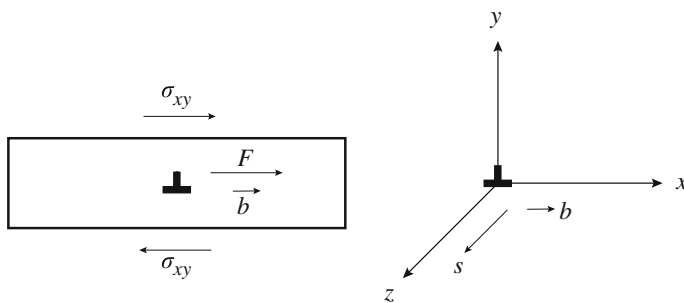
Fig. 7.27 Force on an edge dislocation with character $s|001|$, $b|100|$ due to a shear stress σ_{xy}
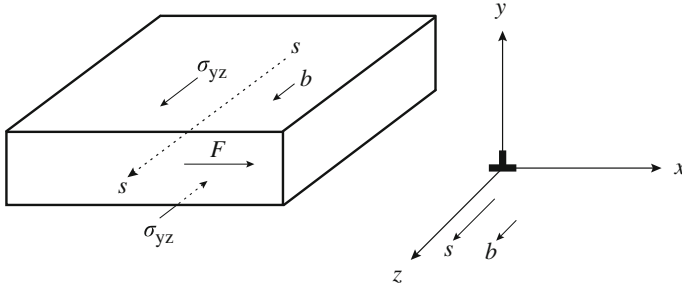
Fig. 7.28 Force on a screw dislocation with character $s|001|$, $b|001|$ due to a shear stress σ_{yz}
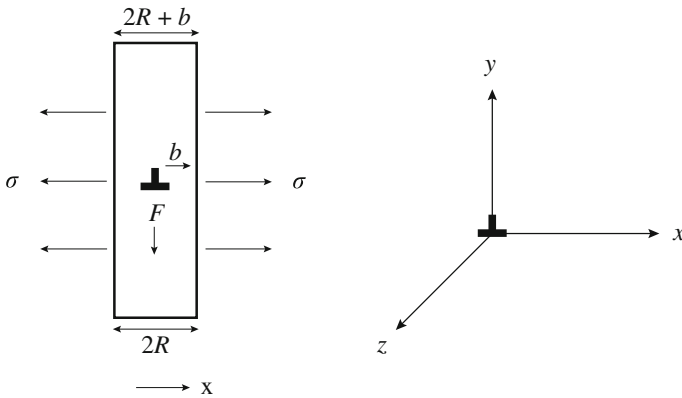
Fig. 7.29 Force on an edge dislocation with character $s|001|$, $b|100|$ due to a normal stress σ_{xx}

Ultimately, we would like to be able to determine the force on any dislocation in a solid subjected to a generalized stress. For example, if we orient a dislocation along the $+z$-direction and its slip plane is perpendicular to the y-axis, then the Burgers vector can be described by:

$$b = b_x i + b_z k, \tag{7.33}$$

where b_x and b_z are edge and screw components of the Burgers vector, and i and k are unit vectors in the x- and z-directions, respectively. This is a mixed dislocation as it's Burgers vector contains components in more than one direction. An external stress placed on the surfaces of a crystal containing a dislocation includes six components: σ_{xx}, σ_{yy}, σ_{zz}, σ_{xy}, σ_{xz}, and σ_{yz}. Of these six stress components, only σ_{yz} and σ_{xy} exert a force on an edge dislocation that will cause motion in the slip plane. Stress components σ_{xz} and σ_{xx} cause motion perpendicular to the slip plane. The

term σ_{zz} does no work, nor does σ_{yy}. The total force on a unit length of dislocation line is then:

$$\boldsymbol{F} = \left(\sigma_{xy}b_x + \sigma_{yz}b_z\right)\boldsymbol{i} - \left(\sigma_{xx}b_x + \sigma_{xz}b_z\right)\boldsymbol{j},\tag{7.34}$$

where the first term is the force component parallel to the slip plane, the second term is the force component normal to the slip plane, and $\boldsymbol{n} = (i, j, k)$ defines the unit vector.

A dislocation of mixed character represents the most general case of a force on a dislocation due to an arbitrary stress field. For a mixed dislocation, the Burgers vector is as follows:

$$\begin{aligned}\boldsymbol{b} &= b_x\boldsymbol{i} + b_y\boldsymbol{j} + b_z\boldsymbol{k} \\ &= b_1\boldsymbol{i} + b_2\boldsymbol{j} + b_3\boldsymbol{k}.\end{aligned}\tag{7.35}$$

Therefore, we write the incremental work done on a dislocation of Burgers vector described by Eq. (7.35) due to an arbitrary stress σ_{ij} as follows:

$$\delta W = \sum_{\substack{i=1 \\ j=1}}^{3} b_i \sigma_{ij} n_j \mathrm{d}A,\tag{7.36}$$

or in matrix notation:

$$\mathrm{d}W = \underline{b}\,\underline{\sigma}\,\underline{n}\mathrm{d}A,\tag{7.37}$$

where $\underline{\sigma}$ is the stress tensor, $\underline{n}$ is the unit vector perpendicular to the slip plane, and $\underline{b}$ is the Burgers vector. Actually, $\underline{b}$ is a column vector so that Eq. (7.37) is written as follows:

$$\mathrm{d}W = \underline{b}^T \underline{\sigma} \cdot \underline{n}\,\mathrm{d}A.\tag{7.38}$$

The term $\underline{n}\,\mathrm{d}A$ can be written as $\mathrm{d}\boldsymbol{A}$ which is just:

$$L(\boldsymbol{s} \times \mathrm{d}\boldsymbol{l}),\tag{7.39}$$

where $\boldsymbol{s}$ is the unit vector in the direction of the dislocation line, L is the length of the dislocation line, and $\mathrm{d}\boldsymbol{l}$ ($=\mathrm{d}x\boldsymbol{i} + \mathrm{d}y\boldsymbol{j} + \mathrm{d}z\boldsymbol{k}$) is the unit vector in the slip plane and is normal to $\boldsymbol{s}$ and $\boldsymbol{n}$ Recall that $\boldsymbol{b} = b_x\boldsymbol{i} + b_y\boldsymbol{j} + b_z\boldsymbol{k}$, so $\boldsymbol{b}$ has a component only in the direction $\mathrm{d}\boldsymbol{l}$. Since $\boldsymbol{A} \cdot \boldsymbol{B} \times \boldsymbol{C} = \boldsymbol{A} \times \boldsymbol{B} \cdot \boldsymbol{C}$, then:

$$\mathrm{d}W = L\underline{b}^T \underline{\sigma} \times \underline{s} \cdot \mathrm{d}\boldsymbol{l},\tag{7.40}$$
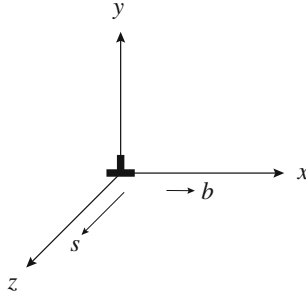
Fig. 7.30 Orientation of an edge dislocation for the determination of the forces due to a generalized stress field

and:

$$\frac{1}{L}dW = \underline{b}^T \underline{\underline{\sigma}} \times \underline{s} \cdot d\boldsymbol{l}. \tag{7.41}$$

The term $\underline{b}^T \underline{\underline{\sigma}} \times \underline{s}$ in Eq. (7.41) is the force per unit length on a dislocation due to an external stress that tends to displace the dislocation, and is designated:

$$\boldsymbol{f} = \underline{b}^T \underline{\underline{\sigma}} \times \underline{s}, \tag{7.42}$$

and is known as the *Peach–Koehler* equation.

Let us apply the Peach–Koehler equation to the case of an edge dislocation described by Burgers vector and direction: $b \begin{vmatrix} 1 \\ 0 \\ 0 \end{vmatrix}$ and $s \begin{vmatrix} 0 \\ 0 \\ 1 \end{vmatrix}$ and shown in Fig. 7.30. We write the first quantity in Eq. (7.42) as follows:

$$\underline{b}^T \underline{\underline{\sigma}} = b|100| \begin{vmatrix} \sigma_{xx} & \sigma_{xy} & \sigma_{xz} \\ \sigma_{yx} & \sigma_{yy} & \sigma_{yz} \\ \sigma_{zx} & \sigma_{zy} & \sigma_{zz} \end{vmatrix} = b| \sigma_{xx} \quad \sigma_{xy} \quad \sigma_{xz} |, \tag{7.43}$$

and then taking the cross product with **s** gives:

$$\underline{b}^T \underline{\underline{\sigma}} \times \underline{s} = b \begin{vmatrix} \boldsymbol{i} & \boldsymbol{j} & \boldsymbol{k} \\ \sigma_{xx} & \sigma_{xy} & \sigma_{xz} \\ 0 & 0 & 1 \end{vmatrix}. \tag{7.44}$$

The cross product, or determinant, is $b\sigma_{xy}\boldsymbol{i} - b\sigma_{xx}\boldsymbol{j}$, and the force on the dislocation is as follows:
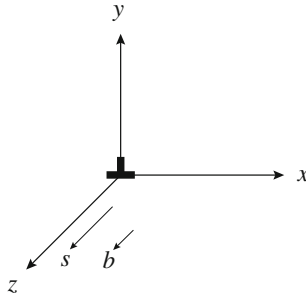
Fig. 7.31 Orientation of a screw dislocation for the determination of the forces due to a generalized stress field

$$\boldsymbol{f} = b\sigma_{xy}\boldsymbol{i} - b\sigma_{xx}\boldsymbol{j}. \tag{7.45}$$

Note that $f_x = b\sigma_{xy}$ is a *glide* force in the +x-direction and the force component $f_y = -b\sigma_{xx}$ is the *climb* force in the $-y$-direction. Only σ_{xy} and σ_{xx} can exert forces on a dislocation with Burgers vector and direction defined as in this example.

For a screw dislocation with Burgers vector and direction given by: $b\begin{vmatrix} 0 \\ 0 \\ 1 \end{vmatrix}$ and $s\begin{vmatrix} 0 \\ 0 \\ 1 \end{vmatrix}$, and shown in Fig. 7.31, we have:

$$\underline{b}^T \underline{\underline{\sigma}} = b|001| \begin{vmatrix} \sigma_{xx} & \sigma_{xy} & \sigma_{xz} \\ \sigma_{yx} & \sigma_{yy} & \sigma_{yz} \\ \sigma_{zx} & \sigma_{zy} & \sigma_{zz} \end{vmatrix} = b| \sigma_{zx} \quad \sigma_{zy} \quad \sigma_{zz} |, \tag{7.46}$$

and then taking the cross product with $\boldsymbol{s}$ gives:

$$\boldsymbol{f} = \underline{b}^T \underline{\underline{\sigma}} \times \underline{s} = b \begin{vmatrix} \boldsymbol{i} & \boldsymbol{j} & \boldsymbol{k} \\ \sigma_{zx} & \sigma_{zy} & \sigma_{zz} \\ 0 & 0 & 1 \end{vmatrix} = b\sigma_{yz}\boldsymbol{i} - b\sigma_{zx}\boldsymbol{j}, \tag{7.47}$$

and $f_x = b\sigma_{zy}$ and $f_y = -b\sigma_{zx}$. Note that only σ_{zy} and σ_{zx} can exert a force on a dislocation defined in this example.

7.1.7 Interactions Between Dislocations

The *Peach–Koehler* equation can also be used to determine the stress on a dislocation due to that from a second dislocation. The difference is that the stress is due
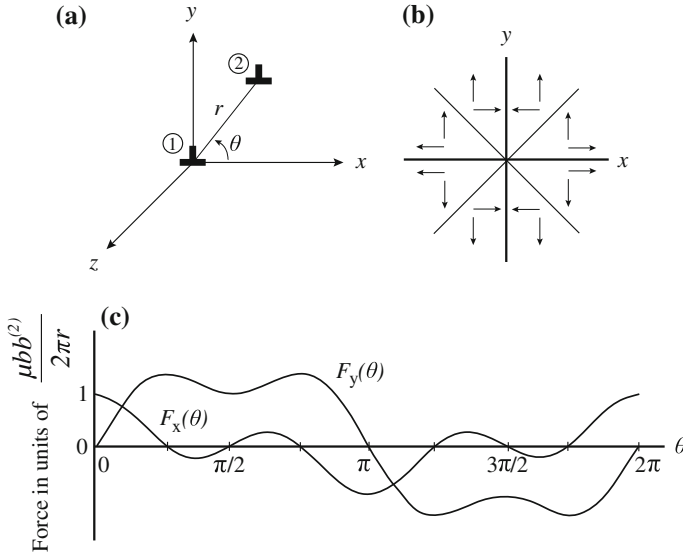
Fig. 7.32 (**a**) Orientation of dislocations to determine the force on edge dislocation (2) due to edge dislocation (1), and *x*- and *y*-components of the force (**b**) in the *x*–*y* plane, and (**c**) as a function of θ

to the presence of the second dislocation rather than external application. We will examine interactions between dislocations by looking at edge–edge, screw–screw, and edge–screw interactions. We will begin with the edge–edge interaction.

Edge–edge interaction

To find the force on dislocation (2) due to the presence of dislocation (1), we locate dislocation (1) at the origin of our coordinate axes and dislocation (2) at some arbitrary position (Fig. 7.32(a)). According to the Peach–Koehler equation, the force is as follows: $\boldsymbol{f} = \underset{(2)}{\underline{b}^T}\ \underset{(1)}{\underline{\underline{\sigma}}} \times \underset{(2)}{\underline{s}}$, where the Burgers vector and direction are those of dislocation (2), and the stress is due to dislocation (1). The first term in the cross product then becomes:

$$\underline{b}^T \underline{\underline{\sigma}} = \underbrace{b|100|}_{(2)}\ \underbrace{\begin{vmatrix} \sigma_{xx} & \sigma_{xy} & 0 \\ \sigma_{yx} & \sigma_{yy} & 0 \\ 0 & 0 & \sigma_{zz} \end{vmatrix}}_{(1)} = b|\ \sigma_{xx}\quad \sigma_{xy}\quad 0\,|, \tag{7.48}$$

and

$$\boldsymbol{f} = \underline{b}^T \underline{\underline{\sigma}} \times \underset{(2)}{\underline{s}} = b\begin{vmatrix} \boldsymbol{i} & \boldsymbol{j} & \boldsymbol{k} \\ \sigma_{xx} & \sigma_{xy} & 0 \\ 0 & 0 & 1 \end{vmatrix} = b\sigma_{xy}\boldsymbol{i} - b\sigma_{xx}\boldsymbol{j}. \tag{7.49}$$

The force on dislocation (2) can be written as:

$$\boldsymbol{F} = \underbrace{\frac{\mu b b^{(2)}}{2\mu(1-v)r}\left(\cos\theta\cos 2\theta\right)\boldsymbol{i}}_{F_x(\theta)} - \underbrace{\frac{\mu b b^{(2)}}{2\pi(1-v)r}\sin\theta(2+\cos 2\theta)\boldsymbol{j}}_{F_y(\theta)}, \qquad (7.50)$$

and the force components in the x–y plane are shown in Fig. 7.32(b), and as a function of θ in Fig. 7.32(c).

Note that if dislocation (2) has the same s but the Burgers vector is in the opposite direction, then the net effect on the resultant force is simply a change in sign of each of the terms in Eq. (7.50) but preservation of the magnitudes. If dislocation (2) has Burgers vector $b\begin{vmatrix} 0 \\ 1 \\ 0 \end{vmatrix}$, then the preceding analysis becomes:

$$\underline{b}^T\underline{\underline{\sigma}} = \underbrace{b|010|}_{(2)}\underbrace{\begin{vmatrix} \sigma_{xx} & \sigma_{xy} & 0 \\ \sigma_{yx} & \sigma_{yy} & 0 \\ 0 & 0 & \sigma_{zz} \end{vmatrix}}_{(1)} = b|\,\sigma_{xy} \quad \sigma_{yy} \quad 0\,|, \qquad (7.51)$$

$$\boldsymbol{f} = \underline{b}^T\underline{\underline{\sigma}} \times \underset{(2)}{\underline{s}} = b\begin{vmatrix} \boldsymbol{i} & \boldsymbol{j} & \boldsymbol{k} \\ \sigma_{xy} & \sigma_{yy} & 0 \\ 0 & 0 & 1 \end{vmatrix} = b\sigma_{yy}\boldsymbol{i} - b\sigma_{xy}\boldsymbol{j}. \qquad (7.52)$$

In this case, the x-component of the force produces a positive climb force to the right, and the y-component of the force produces a negative (downward) glide force.

Screw–screw interaction

For two screw dislocations as shown in Fig. 7.33(a), the force on dislocation (2) due to dislocation (1) is as follows:

$$\boldsymbol{f} = \underline{b}^T\underline{\underline{\sigma}} \times \underset{(2)}{\underline{s}} = b\begin{vmatrix} \boldsymbol{i} & \boldsymbol{j} & \boldsymbol{k} \\ \sigma_{xz} & \sigma_{yz} & 0 \\ 0 & 0 & 1 \end{vmatrix} = b\sigma_{yz}\boldsymbol{i} - b\sigma_{xz}\boldsymbol{j}, \qquad (7.53)$$

where the x-component of the force, $b\sigma_{yz,}$ is to the right, and the y-component of the force, $-b\sigma_{xz,}$ is downward in Fig. 7.33. The force on dislocation (2) can be written as:

$$\boldsymbol{F} = \frac{\mu b b^{(2)}}{2\pi r}\left(\cos\theta\boldsymbol{i} + \sin\theta\boldsymbol{j}\right). \qquad (7.54)$$

The force is in a direction that is perpendicular to the dislocation line. It is repulsive if the dislocations are of the same sign and attractive if the dislocations are of
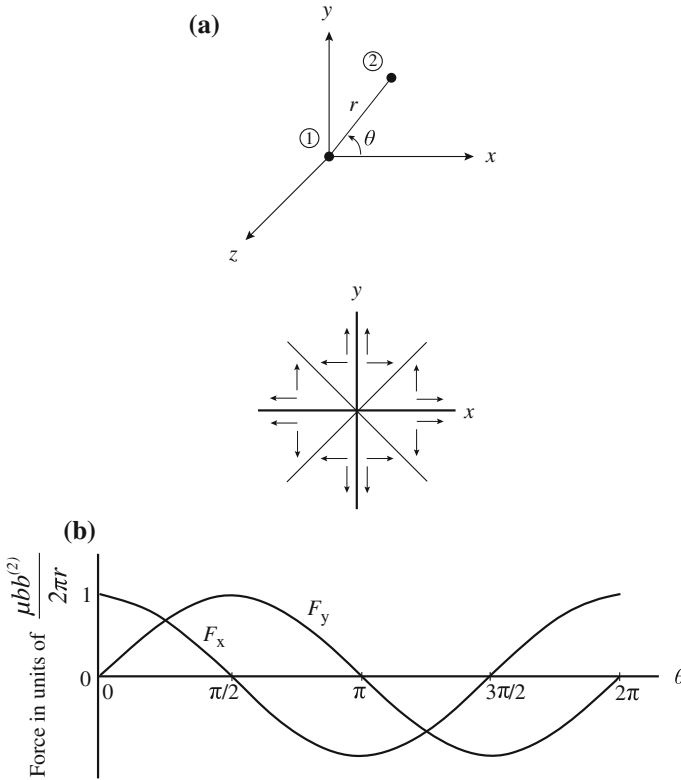
Fig. 7.33 (**a**) Orientation of dislocations to determine the force on screw dislocation (*2*) due to screw dislocation (*1*), and (**b**) the *x*- and *y*-components of the force on a screw dislocation due to another dislocation in the *x*–*y* plane, and (**c**) as a function of θ

opposite sign. The force on the dislocation at the origin due to the dislocation at (r, θ) is equal in magnitude but opposite in sign from the force on the dislocation at (r, θ) due to that at the origin. The force components in the *xy*-plane are shown in Fig. 7.33(b), and the magnitude of the forces as a function of θ are shown in Fig. 7.33(c).

Edge–screw interaction

The last example is the determination of the force between an edge and a screw dislocation as defined in Fig. 7.34. We know that an edge dislocation has no *xz* or *yz* stress components, which are needed to move a screw dislocation. So we can state the following rules: For an edge dislocation with $b \begin{vmatrix} 1 \\ 0 \\ 0 \end{vmatrix}$ and $s \begin{vmatrix} 0 \\ 0 \\ 1 \end{vmatrix}$, the only stresses that produce a force on it are σ_{xx} and σ_{xy}. The stress field around the dislocation has

Fig. 7.34 Orientation of
dislocations to determine the
force on screw dislocation (*2*)
due to edge dislocation (*1*)
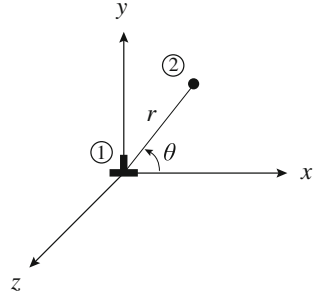
components σ_{xx}, σ_{yy}, $\sigma_{zz,}$ and σ_{xy}. For a screw dislocation with $b \begin{vmatrix} 0 \\ 0 \\ 1 \end{vmatrix}$ and $s \begin{vmatrix} 0 \\ 0 \\ 1 \end{vmatrix}$, the

only stresses that produce a force on it are σ_{xz} and σ_{yz}. The stress field around the
dislocation has components σ_{xz} and σ_{yz}.

7.1.8 Extended Dislocations

Slip occurs in the fcc lattice on (111) planes and in the $\langle 110 \rangle$ direction, as shown in
Fig. 7.35. The Burgers vector is $a/2[110]$, which is the shortest lattice vector con-
necting an atom at the cube corner with a neighboring atom at the center of a cube face.
However, the atom arrangement on the {111} slip plane is such that slip in the [110]
direction is not the easiest path. Figure 7.35(b) shows the atom arrangement on a
close-packed (111) plane. The {111} planes are stacked in the sequence ABCABC…,
such that the centers of the A plane of atoms fall on top of each other, and similarly for
the B and C planes of atoms. The vector $\boldsymbol{b}_1 = a/2\left[10\bar{1}\right]$ shown in Fig. 7.35(b) is the
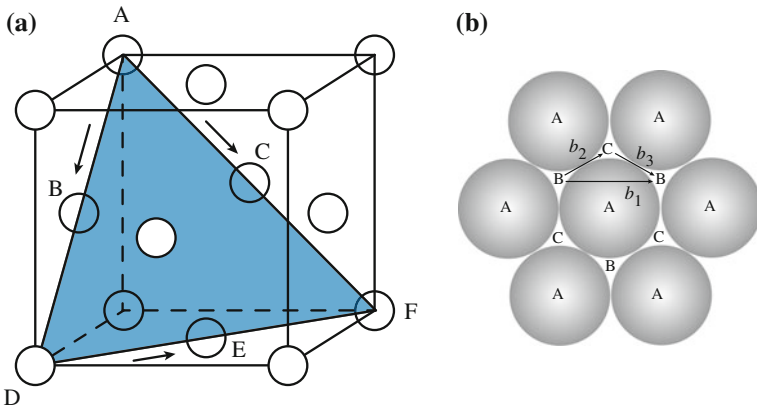
Fig. 7.35 (**a**) Close-packed (111) slip plane in the fcc lattice. (**b**) Slip directions

observed slip direction. However, if atoms are considered as hard spheres, this direction represents a high-energy path as atoms moving from one B site to another must climb over the A atoms. A simpler path is by way of vectors b_2 and b_3, which is along the "valleys" between the A atoms. This dislocation reaction is given by:

$$\boldsymbol{b}_1 \rightarrow \boldsymbol{b}_2 + \boldsymbol{b}_3, \quad a/2[10\bar{1}] \rightarrow a/6[2\bar{1}\bar{1}] + a/6[11\bar{2}]. \tag{7.55}$$

Essentially, the Burgers vector, $\boldsymbol{b}_1$, of the total dislocation has been dissociated into two *partial dislocations* $\boldsymbol{b}_2$ and $\boldsymbol{b}_3$. Figure 7.36(a) shows the atom arrangement of the partial dislocations on the {111} plane, and Fig. 7.36(b) shows the vector diagram of the dissociation of the total dislocation into two partial dislocations. The partials are often called *Shockley partials*, and the combination of the two partials is termed an *extended dislocation*. Dissociation is independent of dislocation character, and the partial dislocations move as a unit that maintains the equilibrium width between them. The space between the partials is referred to as the faulted region or the *stacking fault*, and its size is determined by the *stacking fault energy*, SFE. The lower the SFE, the greater the separation of the partials, and the higher the

Fig. 7.36 Slip on the close-packed (111) plane in the fcc lattice. (**a**) Location of atoms in a Shockley partial. (**b**) Dislocation dissociation into partial dislocations
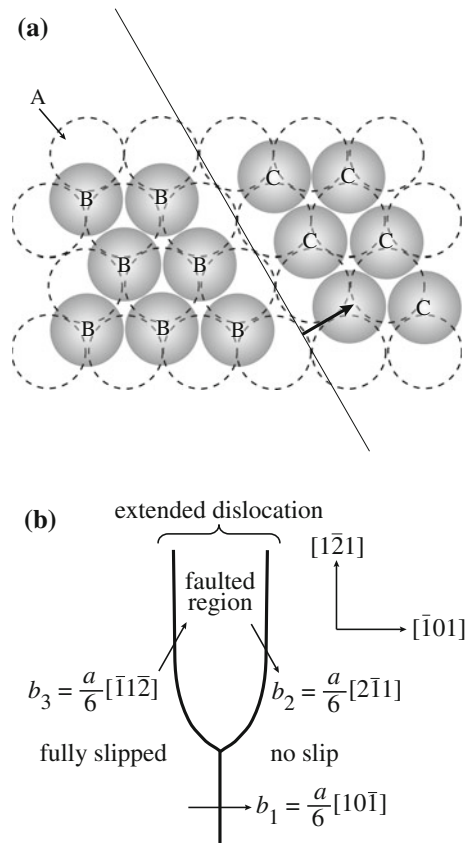
energy, the closer they are together. Stacking faults are important in cross-slip as the partials must recombine for cross-slip to occur. Extended dislocations also occur in hcp lattices, but are not commonly observed in bcc metals.

7.1.9   Kinks and Jogs

Both edge and screw dislocations can acquire jogs or steps in the dislocation line by interaction with other dislocations. The jogs are of two types. A jog that lies in the slip plane instead of normal to it is called a kink. Figure 7.37(a) shows an edge dislocation with a kink of screw character that lies in the slip plane of the edge dislocation, and Fig. 7.37(b) shows a screw dislocation with a kink of edge orientation. Kinks are unstable as they can line up and annihilate during glide. A second type of jog is shown in Fig. 7.37(c) in which the jog and the dislocation are of edge orientation. These types of jogs are able to glide since they lie in the slip plane of the dislocation. The only difference between the motion of the jogged edge dislocation and the ordinary edge dislocation is that instead of gliding along a single plane, it glides over a stepped surface. Another type of jog is the most important in plastic deformation and is shown in Fig. 7.37(d). This is a screw dislocation containing a jog with an edge orientation. The only way the screw dislocation can move to a new position and take its jog with it is by climb of the jog. Figure 7.37(e) shows the movement of a jogged screw dislocation as the segments between jogs bow out in the slip plane under an applied stress producing a trail of vacancies left behind the jog as the dislocation moves in its slip plane.

7.2   Faulted Loops and Stacking Fault Tetrahedra

Because of their importance in irradiated materials, we will discuss Frank loops at greater length. Frank loops are important in irradiated materials because they are often nucleated in a displacement cascade. Recall that the cascade consists of a core of vacancies surrounded by a shell of interstitials (Figs. 3.3 and 3.9). If the vacancy core or the interstitial shell collapses (condenses) onto a close-packed plane, Frank loops may be generated. In both cases, a stacking fault results. Vacancy condensation produces an intrinsic fault, and interstitial condensation results in an extrinsic stacking fault. The faults are described as follows.

In regular, close-packed lattices such as fcc and bcc, atom layers follow a regular stacking sequence. In the fcc lattice, the stacking sequence is ABCABCABC…, indicating that every third layer lies over the first layer. Removal of a layer of atoms results in a break or a fault in the stacking sequence. Removal of a plane of atoms produces an intrinsic stacking fault, which is also known as a single fault, and the dislocations attached to the single fault are S-dislocations, giving an S-Frank dislocation (Fig. 7.38(a)). For example, the sequence is modified to

Fig. 7.37 Kinks and jogs in dislocations. (**a**) Edge dislocation with a kink of screw character. (**b**) Screw dislocation with a kink of edge orientation. (**c**) Edge jog in an edge dislocation. (**d**) Edge jog in a screw dislocation and direction of motion of the dislocation. (**e**) Movement of a jogged screw dislocation of part (**d**) showing bowing of the segments between jogs and the trail of vacancies left behind the trail of jogs (after [7])
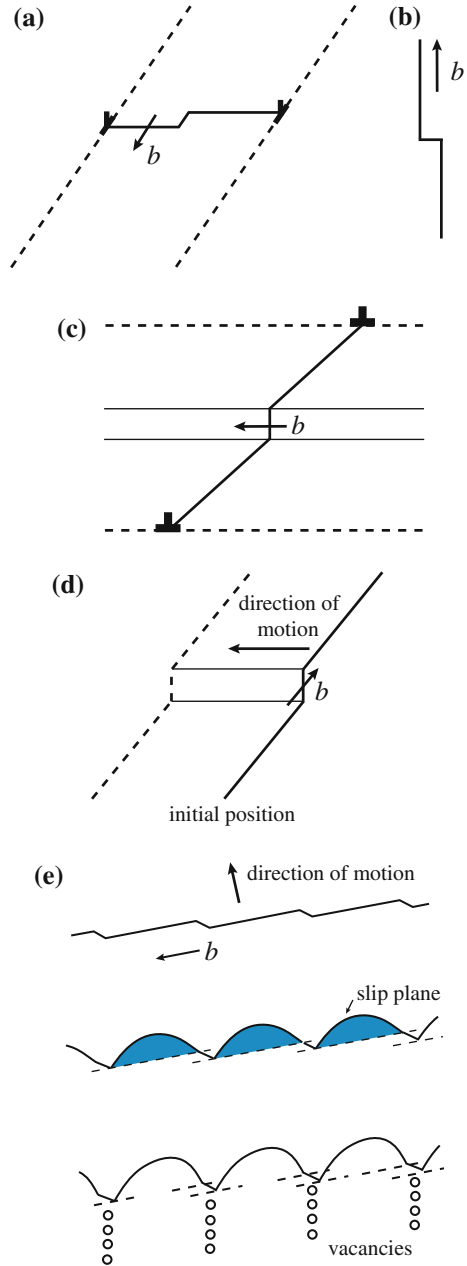
ABCAB/ABCABC…, where "/" denotes the fault or missing plane of atoms. Insertion of an extra plane of atoms produces a double fault in the stacking sequence: ABCAB/A/CABC… (Fig. 7.38(b)). This is an extrinsic or double fault, and the dislocations are D-dislocations giving a D-Frank loop. The Burgers vector
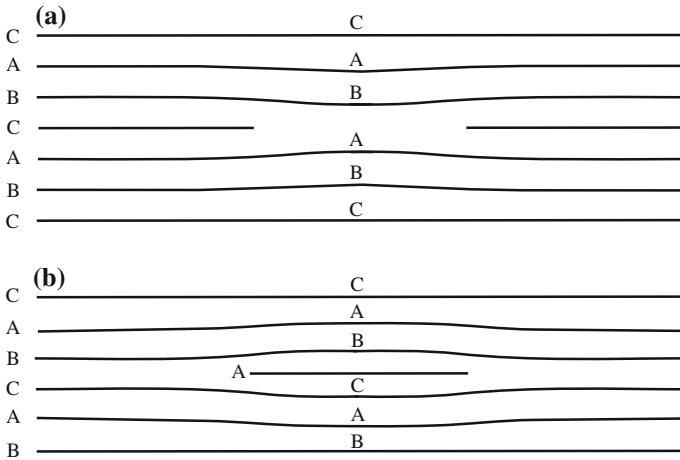
Fig. 7.38 Schematic of (**a**) intrinsic stacking fault and (**b**) extrinsic stacking fault

of the S-Frank and D-Frank loops are identical. Since a Frank loop results from addition or removal of close-packed planes, b must be directed normal to the (111) plane and has a length equal to the spacing between planes, $a/\sqrt{3}$, then the Burgers vector is described by $b = a/3[111]$. Since it is extremely difficult to move on its slip plane (the glide plane is actuallya cylinder defined by the edge of the loop), the Frank loop is considered to be *sessile* or immobile since its glide plane is a *cylinder* defined by the projection of the loop perimeter in a direction perpendicular to, and above or below, the plane of the loop (see Fig. 7.11). A Frank loop can also unfault either autocatalytically or by reaction with a dislocation line to form a perfect loop. This process is described in Chap. 12.

Another dislocation configuration that can form in irradiated metals is the SFT. A SFT is a three-dimensional stacking fault configuration that is in the shape of a tetrahedron. SFTs are believed to evolve directly from vacancy clusters produced in cascades. They are also believed to evolve from Frank loops. A Frank loop will always lie on a (111) plane in an fcc lattice. Figure 7.39(a) shows a loop of triangular shape on a (111) plane with edges parallel to [110] directions. A Frank dislocation that is parallel to a [110] direction can lower its energy by splitting into a Shockley dislocation, $a/6[211]$, and a stair-rod dislocation. The slip plane of the Shockley dislocation is also a (111) plane, but it is different from that containing the Frank loop. Figure 7.39(b) shows two of the three Shockley dislocations formed from the three sides of the Frank loop, moving up (111) planes. Each Shockley has left behind it a stair-rod dislocation, $a/6[110]$, in the position formerly occupied by a side of the Frank dislocation loop (edge of the triangle). The stacking fault contained in the Frank loop now bends at the stair-rod dislocation and extends up onto the close-packed (111) planes of the Shockley dislocations. As the Shockley dislocations move up the planes shown in Fig. 7.39(b), they eventually meet at the intersections of their slip planes and the intersections of Shockley dislocations result

Fig. 7.39 A stacking fault tetrahedron (SFT) formed by faults on each of the faces of the tetrahedron (after [1])
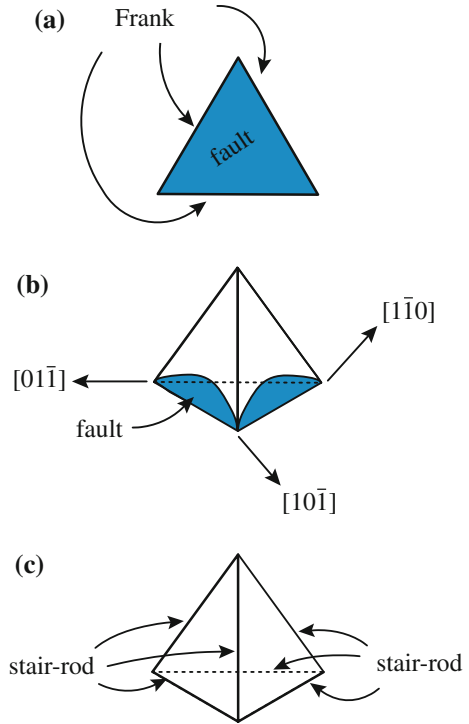
in other stair-rod dislocations along the remaining three edges of the tetrahedron. The final configuration is a tetrahedron whose sides are stacking faults and whose edges are stair-rod dislocations (Fig. 7.39(c)). The Frank dislocation and the Shockley dislocations no longer exist.

Dislocations can also interact with SFTs. MD simulation of the interaction of a dissociated $a/2[110]$ dislocation (into two Shockley partials, $a/6[121]$) on the (111) glide plane shows that several types of interaction are possible [8]. When the SFT is in the slip plane of the dislocation, the SFT may be cut by the dislocation and recovers by a shift of the structure above the glide plane to regain its original shape. The interaction can also create ledges in the SFT that can reduce stability and lead to dissolution. TEM observations show that SFTs can be cut multiple times by dislocations in channels.

7.3 Defect Clusters

As described in Chap. 3, the fraction of defects produced in a cascade is between 20 and 40 % of that predicted by the NRT model due to intracascade recombination. Of these, not all appear as single interstitial atoms or isolated vacancies. A

significant fraction of defects are created in the form of clusters, rather than as single defects. Vacancy clusters may grow to form voids, which are an important microstructure feature that influences both dimensional (Chap. 8) and mechanical (Chap. 12) properties of materials. If the clusters are stable, they may also migrate away from the cascade region and be absorbed at sinks such as dislocations and grain boundaries. Interstitial and vacancy clusters must be treated separately since in general, interstitial clusters are stable and vacancy clusters are not. Their mobilities differ as well with interstitial clusters exhibiting greater mobility than their vacancy counterparts.

7.3.1   Fraction of Defects Forming Clusters

In-cascade clustering of defects is important because it promotes nucleation of extended defects. Interstitial clustering can occur in one of two ways. In the first, interstitial clusters are created in the transition between the collisional and thermal spike phases in which atoms that are displaced from the cascade center due to the initial shock wave are pushed into interstitial locations. Alternatively, clusters can occur during the thermal spike phase by short-range diffusion driven by the elastic interaction between neighboring interstitials. The probability of clustering and the size of the clusters tend to increase with increasing PKA energy, and a higher proportion of SIAs form clusters than do vacancies [9]. Figure 7.40 shows the fraction of interstitials that form clusters as a function of the PKA energy in several metals and, at 100 K, as determined by MD simulation [10]. Note that the clustered fraction increases quickly with T as damage transitions from single displacements to cascade morphology. In contrast to the Frenkel pair production efficiency (Fig. 3.21), the clustered fraction varies with the metal, and while there are only 5 metals shown here, the clustering appears to occur according to the crystal structure with the highest

Fig. 7.40 The fraction, f_i^{cl}, of SIAs that survive as clusters containing at least two interstitials in several metals and Ni_3Al at 100 K (after [10])
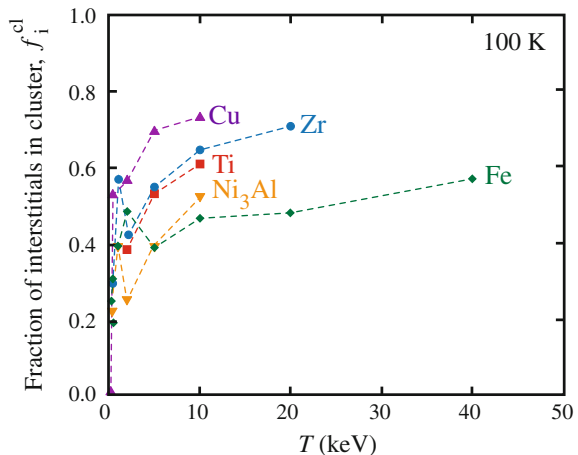
clustering fraction occurring for the fcc structure and the lowest for the bcc structure with the hcp structure in between.

Note from Fig. 7.40 that with continued increase in T, the cluster fraction saturates. This is likely due to the fact that very high-energy cascades break up into several subcascades that resemble those at lower energy. As such, the surviving defect fraction and the clustering fraction plateau at values representative of the lower energy cascades. An example of subcascade formation is shown in Fig. 7.41 for a 100 keV cascade in 100 K iron where 5 and 10 keV cascades have been superimposed into the same block of atoms for comparison.

While MD results show that the fraction of interstitials in clusters is larger in copper than in α-iron by $\sim$70–45 % at 100 and 600 K for PKA energies above 5 keV [12], experimental evidence shows that the cluster density in copper is as much as 10^3 higher than that in Fe [13]. While the size of this difference is not understood, it may have its origins in the nature of the cluster as discussed in the next section.

The dependence of in-cascade interstitial clustering on cascade energy is shown in Fig. 7.42 for MD simulation temperatures of 100, 600, and 900 K, where the average number of interstitials in clusters of size two or larger at each energy has been divided by the total number of surviving interstitials in Fig. 7.42(a) and by the number of displaced atoms predicted by the NRT model for that energy in Fig. 7.42(b). Note that

MD cascade simulations in iron at 100K: peak damage

5 keV: 0.26 ps
10 keV: 0.63 ps
100 keV: 0.70 ps
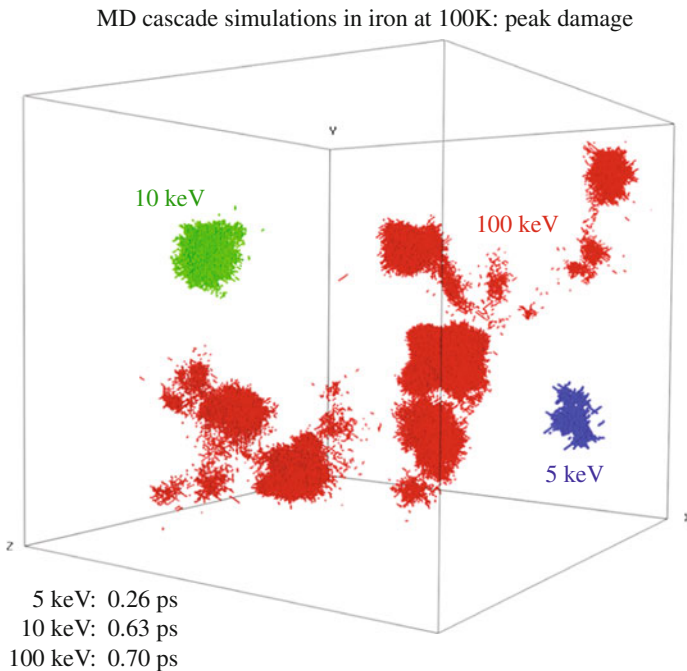
Fig. 7.41 Energy dependence of subcascade formation (after [11])

Fig. 7.42 Fraction of surviving interstitials contained in clusters (**a**) relative to the total number of MD defects created and (**b**) relative to the NRT displacements (after [11])
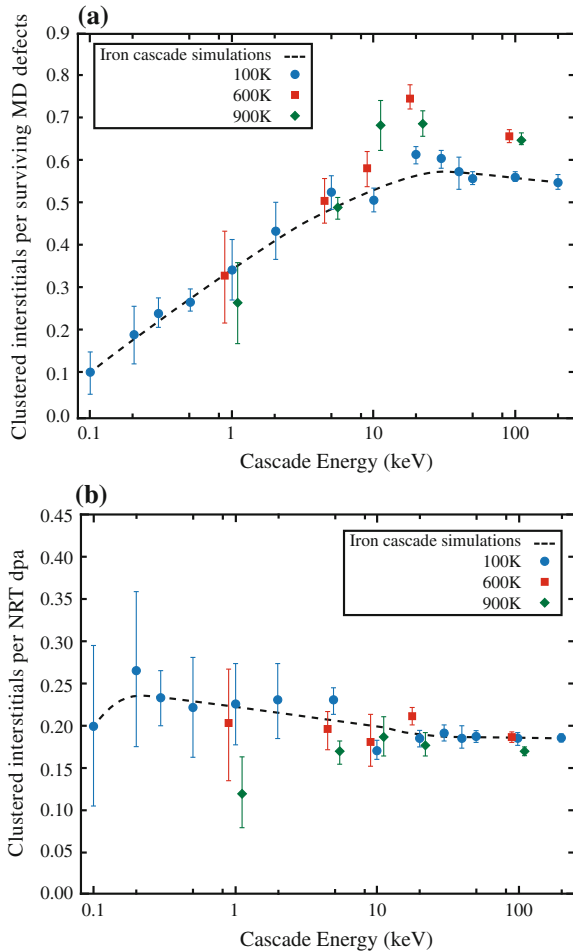
the relative scatter is much higher at lower energies, which is similar to the case of defect survival shown in Fig. 3.17. The average fraction of interstitials in clusters is about 20 % of the NRT displacements above 5 keV, which corresponds to about 60 % of the total surviving interstitials. Although it is not possible to discern a systematic effect of temperature below 10 keV, there is a trend toward greater clustering with increasing temperature at higher energies. This can be more clearly seen in Fig. 7.42a where the ratio of clustered interstitials to surviving interstitials is shown. Interstitial clustering increases at higher temperatures due to the more compact nature and longer lifetime of the cascade at higher temperature, providing more time for interstitials to diffuse and interact. Recall from Sect. 3.6 and Fig. 3.22 that the Frenkel pair production decreases slightly with temperature. Combining these results, the effect of temperature can be described as resulting in an increasing fraction of the decreasing

population of interstitials forming clusters as the temperature increases, yielding a net increase in f_i^{cl}. This effect of temperature on interstitial clustering is consistent with the observations of increasing interstitial clustering fraction with temperature [14].

The clustered fraction can be broken down according to cluster size to reveal the dependence of clustering on cluster size. Figure 7.43 shows the fraction of SIAs in clusters of sizes $\simeq 2$, $\simeq 3$, and $\simeq 4$ in copper as a function of damage energy for an irradiation temperature of 100 K. Note that the cluster fraction is very sensitive to minimum cluster size, especially at lower damage energies, yielding a net decrease in f_i^{cl}.

Clustering of vacancies occurs within the core of the cascade as well, and the extent of clustering varies with the host lattice. Based on the measurements of size and number density of vacancy clusters in irradiated metals, the fraction of vacancies in clusters is estimated to be less than 15 %. The energy and temperature dependence of in-cascade vacancy clustering as a fraction of the NRT displacements is shown in Fig. 7.44 for cascade energies of 10–50 keV. Results are shown for clustering criteria of first, second, and fourth nearest neighbor, NN. A comparison of Figs. 7.42(b) and 7.44 demonstrates that in-cascade vacancy clustering in iron remains lower than that of interstitials even when the fourth NN criterion is used. This is consistent with experimentally observed difficulty of forming visible vacancy clusters in iron and the fact that only relatively small vacancy clusters are found in positron annihilation studies of irradiated ferritic alloys [15]. The true fraction may be larger because of the invisibility of small clusters, but also the fact that vacancy clusters are not nearly as stable as interstitial clusters as will be shown in the next section. The cascade energy dependence of vacancy clustering is similar to that of interstitials; there is essentially zero clustering at the lowest energies, but it rapidly increases with cascade energy and is

Fig. 7.43 The fraction f_i^{cl}, of SIAs that survive in clusters of two or more, three or more, and four or more in copper at 100 K (after [10])
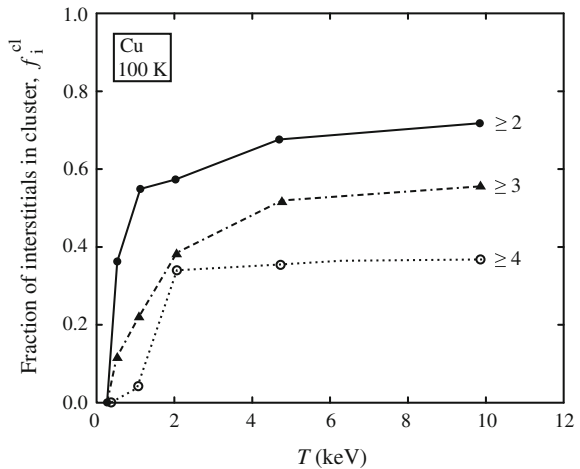
Fig. 7.44 Cascade energy dependence of vacancy clustering described by the number of clustered vacancies divided by NRT displacements (after [11])
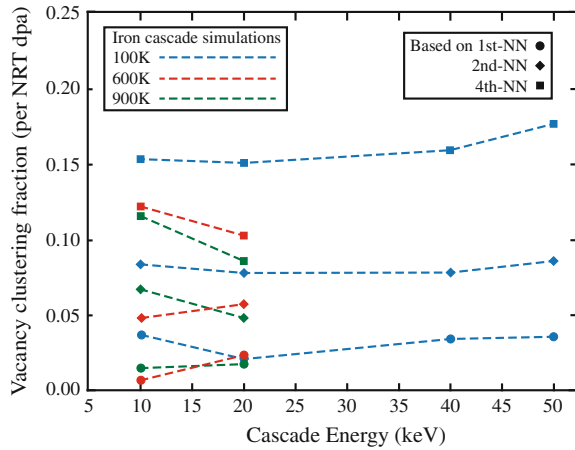
relatively independent of energy above ~ 10 keV. However, vacancy clustering decreases as the temperature increases, which is consistent with vacancy clusters being thermally unstable.

7.3.2 Types of Clusters

The structure of the cluster is a strong function of the crystal structure [13, 16]. In α-Fe, MD simulation shows that the most stable configuration of small clusters (<10 SIAs) is a set of ⟨111⟩ crowdions. Next in stability is the ⟨110⟩ crowdion. As the cluster size grows (>7 SIAs), only two configurations are stable, the ⟨111⟩ and ⟨110⟩ crowdions. These crowdions also may act as nuclei for the formation of perfect interstitial dislocation loops with Burgers vector 1/2⟨111⟩ or ⟨100⟩, respectively.

In fcc copper, the ⟨100⟩ dumbbell is the stable configuration of the SIA and the smallest cluster is of the form of two ⟨100⟩ dumbbells. Larger clusters can have two configurations: a set of ⟨100⟩ dumbbells or a set of ⟨110⟩ crowdions, each with {111} as the habit plane. During growth, the clusters transform into faulted Frank loops with Burgers vector 1/3⟨111⟩ and perfect loops with Burgers vector 1/2 ⟨110⟩. The binding energy of SIA loops in Fe and in Cu is shown in Fig. 7.45(a, b), respectively. Note that the binding energy for SIA loops in Cu is slightly higher than for SIA loops in α-Fe, in agreement with the higher clustering fraction predicted by MD modeling. Figure 7.46 shows a micrograph of interstitial clusters and small interstitial loops in a copper foil after irradiation with 30 keV Cu^+ ions. Note that these defect clusters are only a few nanometers in size. Cluster densities can reach very high levels as shown in Fig. 7.47.

Fig. 7.45 Binding energy for
SIA loops of different shapes
and Burgers vectors (**a**) in
α-Fe and (**b**) in copper
(after [13])
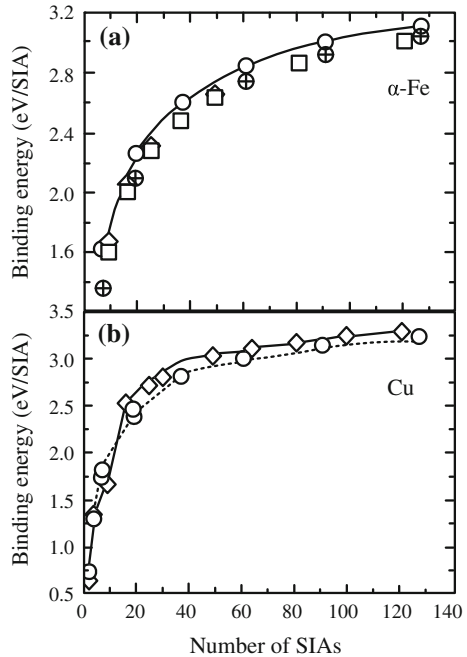
The stability of vacancy clusters is low relative to interstitial clusters. The most stable configurations for vacancy clusters in α-Fe are either a set of divacancies concentrated on two adjacent {100} planes, or a set of first nearest neighbor vacancies on a {110} plane. During cluster growth, the first type results in a perfect dislocation loop with Burgers vector ⟨100⟩ and the second unfaults into a perfect loop with Burgers vector 1/2⟨111⟩. Vacancy loops can also exist in the faulted configuration. The loops will generally unfault to form perfect loops when the number of vacancies reaches about 40 [12].

In fcc Cu, the most stable configurations of a vacancy cluster are the SFT and faulted clusters on {111} planes that form Frank loops with Burgers vector 1/3 ⟨111⟩. Binding energies of the various vacancy configurations in α-Fe and Cu are shown in Fig. 7.48(a, b). Note that the binding energy of vacancies in the cluster is much less than that for interstitials shown in Fig. 7.45(a, b). The binding energy per defect for a four-defect cluster is less than 0.4 eV for vacancies, but is about 1.2 eV for interstitials. Observation by transmission electron microscopy [18] reveals that vacancy dislocation loops and SFT a few nanometers in size are formed by cascades in many metals (Fig. 7.49).

Fig. 7.46 Micrograph of
interstitial clusters and small
interstitial loops in copper
irradiated with 30 keVCu$^+$.
Defects are highlighted by the
circles on the micrographs
(after [17])
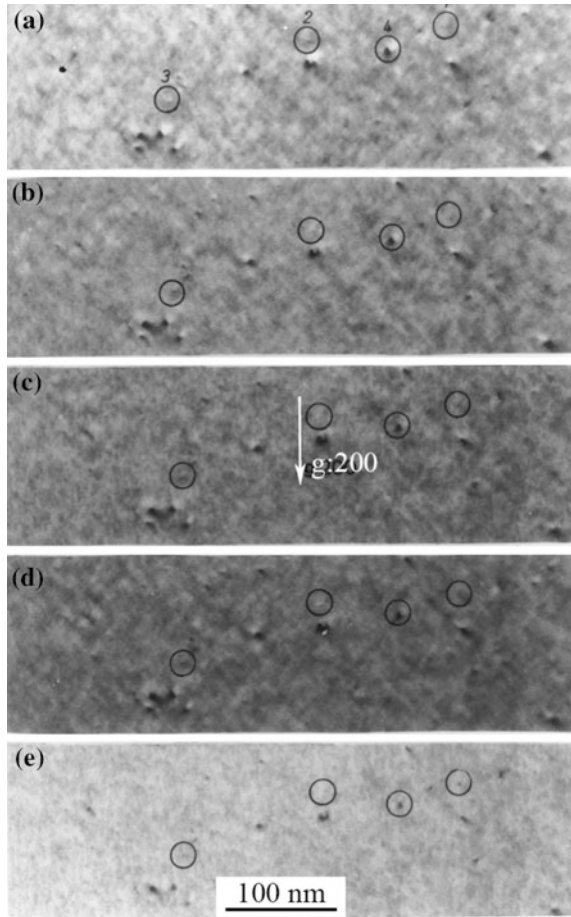
Fig. 7.47 Dose dependence
of cluster densities measured
in α-iron and copper irradiated
with fission neutrons at
temperatures below 0.3 T_m
(after [13])
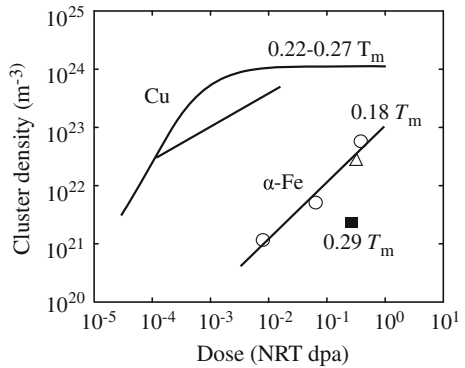
Fig. 7.48 Binding energy of vacancy loops of different shapes and Burgers vectors in (a) α-Fe and (b) copper (after [13])
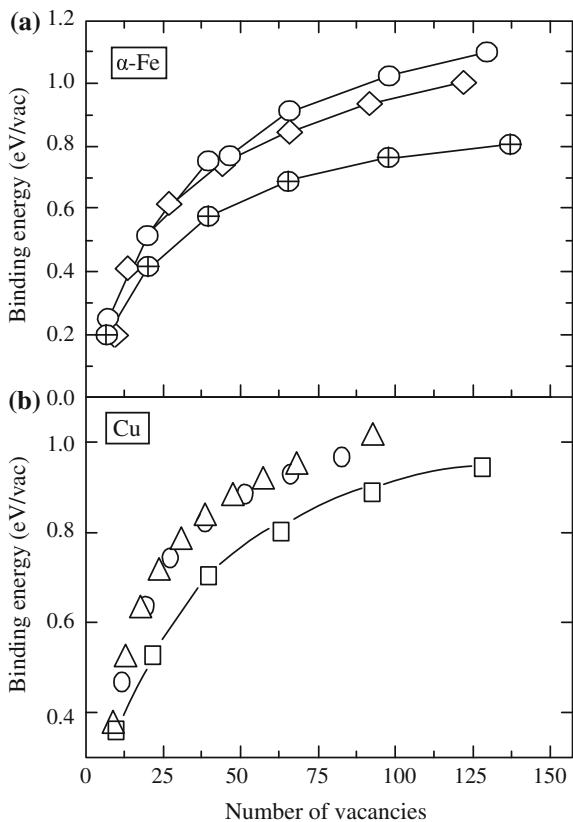
Fig. 7.49 Transmission electron micrograph of (a) defect clusters in gold irradiated to 1.1×10^{22} n/m^2 at 200 °C and (b) stacking fault tetrahedra in silver irradiated to 4.4×10^{21} n/m^2 at 400 °C (after [18])
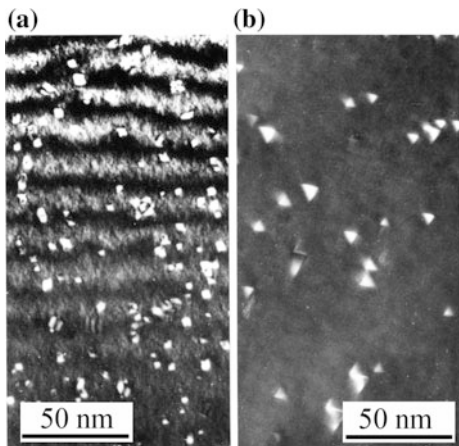
7.3.3 Cluster Mobility

SIA created in the collision cascades of energetic recoil atoms in metals can form as crowdions and clusters of coupled crowdions along close-packed directions. These crowdions and clusters (essentially small, perfect dislocation loops) can migrate in one-dimensional (1D) random walks by thermally activated glide with a very low activation energy (< 0.1 eV) [19]. Movie 7.1 (http://rmsbook2ed.engin.umich.edu/movies/) shows cluster formation and 1D glide in UHP iron irradiated with 150 keV Fe ions at 400 °C. Clusters are just beginning to nucleate in this real-time recording shown at 2× actual time. Compared to defects migrating in 3D, the SIA and SIA clusters migrating in 1D have a much smaller probability of interacting with other defects within the cascade region. Clusters migrating by 1D glide can change their Burgers vectors by thermal activation or by interaction with another defect and continue their 1D glide along another close-packed direction. The result is a 3D diffusion path that is made up of segments of 1D glide, which is referred to as "mixed 1D/3D" defect migration and shown in Fig. 7.50.

(a) 3-D: lattice spacing **(b)** Pure 1-D

(d) Preferentially 1-D: $D_z \gg D_r$

(c) Mixed 1-D/3-D: average length L between direction changes
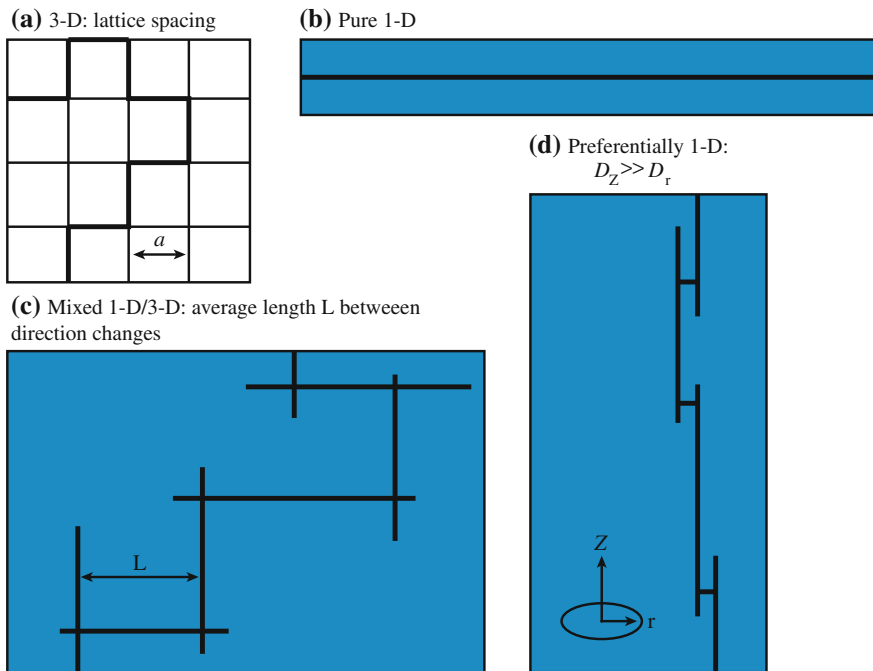
Fig. 7.50 Schematic illustration of defect migration paths by (**a**) 3D random walk on the crystal lattice, (**b**) 1D random walk, (**c**) mixed 1D/3D migration consisting of a 3D path made up of segments of 1D random walks in different random close-packed directions, and (**d**) preferential 1D migration consisting of segments of 1D random walks in the same direction broken by occasional hops to adjacent atom rows (after [20])

However, not all clusters are glissile. Besides stable, faulted Frank loops, SIAs may form metastable arrangement of SIAs that do not reorganize into a stable, glissile form by the end of the thermal spike. They are significant because if they do not migrate away from the cascade, they may act as nucleation sites for the growth of extended defects. Figure 7.42 indicates that the fraction of SIA clusters in a metastable sessile configuration by the end of the thermal spike phase is between 10 and 30 %. The form of these clusters varies with crystal structure. In hcp metals, small sessile clusters form a triangular arrangement of closely packed atoms on the basal plane. In α-iron, three SIAs can form a triangle that is parallel to but displaced from the {111} plane. If clusters form as faulted dislocation loops, such as $b = 1/3 \langle 111 \rangle$ in fcc, $1/2\langle 110 \rangle$ in bcc, and $1/2\langle 0001 \rangle$ in hcp, then they are intrinsically sessile and cannot exhibit glide. The ability to move arises from the clustered crowdion form of these extended defects. They have a form best described as small perfect interstitial dislocation loops with Burgers vector $b = 1/2\langle 110 \rangle$ in fcc, $1/2\langle 111 \rangle$ and $\langle 100 \rangle$ in bcc, and $1/3\langle 11\bar{2}0 \rangle$ in hcp. Table 7.1 summarizes the Burgers vectors of the glissile and sessile dislocation loops formed by vacancy and interstitial clusters.

Mobile clusters can interact with other clusters or with impurity atoms such as helium. The behavior of small interstitial clusters in the presence of impurity helium atoms and vacancies is illustrated in Movies 7.2–7.4 (http://rmsbook2ed.engin. umich.edu/movies/). In Movie 7.2, a SIA (green spheres) in bcc iron interacts with two substitutional He (light blue spheres) atoms and the interaction leads to recombination and ejection of the He into an interstitial position from which it migrates and traps the other He substitutional atom. Movie 7.3 shows the interaction between a 6-SIA cluster and three substitutional He atoms. In this case, recombination and He ejection occurs with two of the three He atoms resulting in a cluster consisting of 4-SIA and one interstitial He atom, and a cluster consisting of one interstitial He and one substitutional He. Movie 7.4 shows the interaction between a 6-SIA cluster and a 4-He/6-vacancy cluster. Vacancies are denoted by the red spheres. The interaction causes the recombination and rejection of He resulting in a 4-He/1-SIA cluster.

Table 7.1 Summary of Burgers vectors of glissile and sessile loops in fcc, bcc, and hcp lattices (after [10])

Crystal structure	Burgers vector	Cluster mobility
fcc	$b = 1/2\langle 110 \rangle$	Glissile
	$b = 1/3\langle 111 \rangle$	Sessile
	SFT (vacancy)	Sessile
bcc	$b = 1/2\langle 111 \rangle, \langle 100 \rangle$	Glissile
	$b = 1/2\langle 110 \rangle$	Sessile
hcp	$b = 1/3\langle 11\bar{2}0 \rangle$	Glissile
	$b = 1/2\langle 10\bar{1}0 \rangle, 1/2\langle 0001 \rangle$	Sessile

   The majority of SIA clusters are glissile. Di- and tri-interstitial clusters in both
α-iron and copper undergo one-dimensional glide along the crowdion direction
[13]. In these small clusters, the crowdion can rotate such that glide occurs in an
equivalent direction. This rotation results in essentially three-dimensional motion.
The rotation frequency is lower for tri-interstitials and increases with temperature
for both defects. Larger clusters are essentially perfect dislocation loops with a
Burgers vector along the crowdion axis, so that their movement can be considered
as thermally assisted glide in one dimension. Figure 7.51 shows 19- and
91-interstitial clusters in α-iron. Both loops extend over six (220) planes as shown
in the figures at the right of each cluster. The motion of these clusters is
one-dimensional and along $\langle 111 \rangle$. A feature of cluster motion is that the effective
correlation factor is greater than unity, i.e., a cluster that has moved one step has a
high probability of making the next step in the same direction. Movie 7.5 is an MD
simulation of a 19-SIA cluster in bcc iron at 287 °C. The cluster exhibits
one-dimensional motion in the direction of the Burgers vector.

(a)   **(b)**   **(c)**
$[11\bar{1}]$ projection   representation of
19-member SIA cluster   [001] projection   (220) planes

91-member SIA cluster
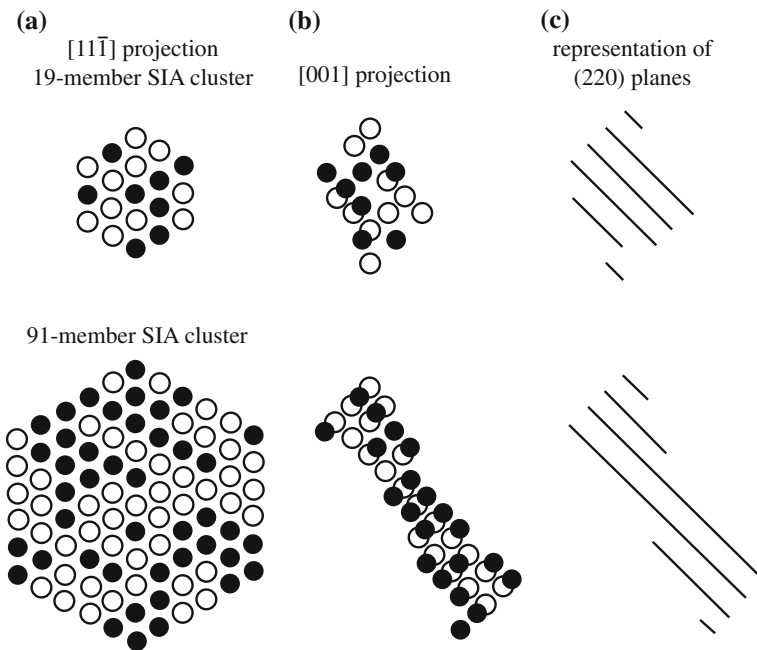
Fig. 7.51   A 19- and 91-interstitial cluster in (**a**) $[11\bar{1}]$ and (**b**) [001] projections. Filled and open
circles represent the centers of mass of $\langle 111 \rangle$ crowdions and split dumbbells, respectively.
(**c**) Additional (220) lattice planes occupied by the clusters (after [21])

The activation energy for cluster motion is between 0.022 and 0.026 eV in α-iron and between 0.024 and 0.030 eV in copper [13]. The activation energy is weakly dependent on the size of the cluster, allowing the cluster jump frequency to be expressed as:

$$v_n = v_0 n^{-s} \exp(-\langle E_m \rangle / kT), \tag{7.56}$$

where $\langle E_m \rangle$ is the average effective activation energy, v_0 is the size-independent, pre-exponential factor, and the term n^{-s} is the cluster size dependence, where a value of ~ 0.65 for s describes the cluster size dependence of the pre-exponential factor for both α-iron and copper. Figure 7.52 shows the total pre-exponential factor as a function of cluster size. This dependence is likely due to enhanced focusing of the crowdion configuration for SIAs in a cluster, which results in increased probability of successive jumps.

Observations have shown that the mobility of clusters depends on the composition. When chromium is added to iron, cluster mobility is significantly reduced. Movie 7.6 shows a comparison of loop hopping in UHP Fe and Fe-8 %Cr under the same irradiation conditions of 150 keV Fe ions at 300 °C. Note that 1D loop motion is evident in pure iron, but relatively rare in Fe-8 %Cr.

Fig. 7.52 Size dependence of the pre-exponential factor in Eq. (7.56) in (**a**) α-Fe and (**b**) Cu (after [13])
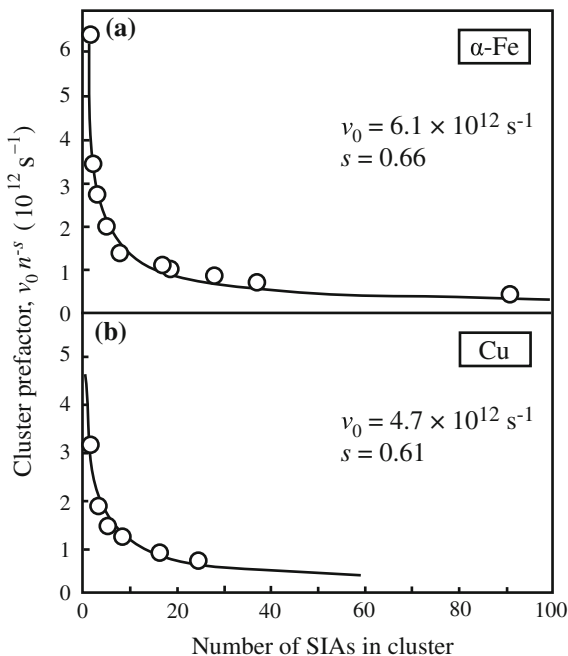
Fig. 7.53 Jump frequency versus reciprocal temperature for vacancy loops (*squares* and *diamonds*) and SIA loops (*circles*) in Fe at 375 °C (after [13])
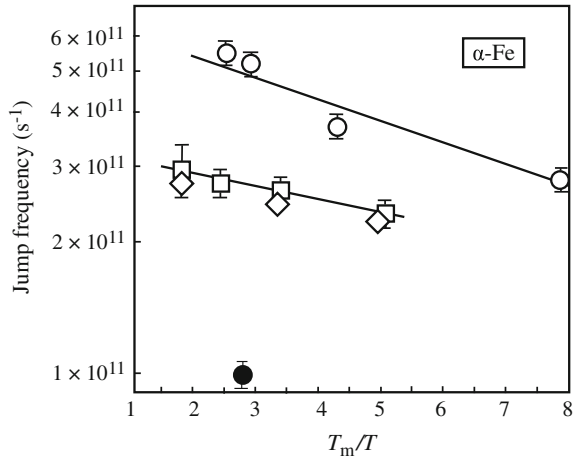
Vacancy clusters that form perfect dislocation loops are also intrinsically glissile. MD simulation shows that the mobility of perfect vacancy loops with $b = 1/2\langle110\rangle$ and $1/2\langle111\rangle$ in Cu and α-iron, respectively, is only slightly lower than that of a cluster of the same number of interstitial crowdions [13]. The result is shown in Fig. 7.53 for a 37-defect cluster. As long as they are in the form of perfect loops, they are mobile. Vacancy clusters that do not collapse to a dislocation structure or that form a Frank loop or SFT are immobile.

7.4 Extended Defects

As described in the previous sections, vacancies and interstitials can cluster to form other types of defects that will be important in defining the effect of irradiation on both physical and mechanical properties of the solid. In principle, a cluster of point defects could be one-dimensional (a line), two-dimensional (a disk), or three-dimensional (a void). Vacancies and interstitials that cluster in numbers greater than those discussed earlier will agglomerate into specific configurations in the crystal lattice. In particular, they will take up the minimum energy configuration, which in three dimensions is a void and in two dimensions is a loop or platelet with a thickness of magnitude equal to one Burgers vector and lying between adjacent close-packed planes.

It may be envisioned that following the radiation damage event, the core of the displacement spike collapses (or the vacancies condense) onto the {111} plane, forming a vacancy disk. The energy of the disk can be written as:

$$E_d = 2\pi r_d^2 \gamma, \tag{7.57}$$

where r_d is the disk radius, and γ is the surface energy of the metal. For a small number of vacancies, the aggregate form with the least energy is the spherical void. The energy of the spherical void of radius r_V is:

$$E_V = 4\pi r_V^2 \gamma. \tag{7.58}$$

If Ω is the atomic volume, then the number of vacancies in the void is as follows:

$$n_v = \frac{4}{3} \frac{\pi r_V^3}{\Omega}. \tag{7.59}$$

The energy of the void written in terms of the number of vacancies, n_v, is as follows:

$$E_V = 4\pi \left(\frac{3n_v\Omega}{4\pi}\right)^{2/3} \gamma = (6n_v\Omega\sqrt{\pi})^{2/3}\gamma. \tag{7.60}$$

For a large number of vacancies, the planar loop is a more stable configuration and this will be discussed shortly.

Another possible configuration of a cluster of vacancies is the SFT as described in Sect. 7.2. The energy of the SFT is given by [4, 22, 23]:

$$E_{SFT} = \frac{\mu L b^2}{6\pi(1-v)}\left[\ln\left(\frac{4L}{a}\right) + 1.017 + 0.97v\right] + \sqrt{3}\overline{L}^2\gamma_{SFE}, \tag{7.61}$$

where v is Poisson's ratio, a is the lattice parameter, γ_{SFE} is the energy of the stacking fault, and L is the length of the edge of the tetrahedron and $L = a(n_v/3)^{1/2}$.

A similar process involving interstitial condensation may occur around the edges of the depleted zone where high interstitial concentrations may exist. The condensation of interstitials onto a close-packed plane produces an extra layer of atoms and two breaks in the stacking sequence, as described in Sect. 7.2. For a disk of radius r_L, the energy of a faulted loop (vacancy or interstitial) is as follows:

$$E_L = 2\pi r_L \Gamma + \pi r_L^2 \gamma_{SFE}, \tag{7.62}$$

where the first term is the energy of the dislocation line, the second term is the energy associated with the stacking fault, and Γ is the energy per unit length of dislocation line. In the fcc lattice, faulted loops lie on the $\{111\}$ planes, which have an atom density of $4/\sqrt{3}a^2$, or an area per atom of $\sqrt{3}a^2/4$. So the radius of a loop consisting of n vacancies (or interstitials) is as follows:

$$r_L = \left(\frac{\sqrt{3}a^2n}{4\pi}\right)^{1/2}. \tag{7.63}$$

Approximating Γ with μb^2, Eq. (7.32b) where μ is the shear modulus and b is the Burgers vector, Eq. (7.62) becomes:

$$E_L = 2\pi\mu b^2 \left(\frac{\sqrt{3}a^2 n}{4\pi}\right)^{1/2} + \pi\left(\frac{\sqrt{3}a^2 n}{4\pi}\right)\gamma_{SFE}. \tag{7.64}$$

More precise expressions for the energy of faulted and perfect loops are given in [4, 6, 22–24], and from [24], the energy of the faulted Frank loop is as follows:

$$E_F = \frac{2}{3}\frac{1}{(1-v)}\mu b^2 r_L \ln\left[\frac{4r_L}{r_c} - 2\right] + \pi r_L^2 \gamma_{SFE}. \tag{7.65}$$

The energy of a perfect loop [18] is as follows:

$$E_P = \frac{2}{3}\frac{1}{(1-v)} + \frac{1}{3}\left(\frac{2-v}{2(1-v)}\right)\mu b^2 r_L \ln\left[\frac{4r_L}{r_c} - 2\right], \tag{7.66}$$

where r_c is the dislocation core radius. Equations (7.65) and (7.66) refer to both interstitial and vacancy loops, and from these equations, the difference in energy between a perfect loop and a Frank loop is as follows:

$$\Delta E = \pi r_L^2 \gamma_{SFE} - \frac{1}{3}\left(\frac{2-v}{2(1-v)}\right)\mu b^2 r_L \ln\left[\frac{4r_L}{r_c} - 2\right]. \tag{7.67}$$

Therefore, unfaulting is favorable if:

$$\gamma_{SFE} > \frac{\mu b^2}{3\pi r_L}\left(\frac{2-v}{2(1-v)}\right)\ln\left[\frac{4r_L}{r_c} - 2\right]. \tag{7.68}$$

Equations for a disk, void, perfect loop, faulted loop, and SFT are plotted in Fig. 7.54(a, b) for 316 stainless steel and zirconium, respectively. The values of the material parameters are provided in the caption. Note that in general faulted defects are more stable in zirconium than in stainless steel, and voids are more stable in stainless steel than in zirconium. In stainless steel, voids are stable to relatively large sizes and the energy of the faulted loop remains below that of the perfect loop to large defect sizes. In zirconium, faulted loops and SFTs are more stable than voids. The high susceptibility to void swelling in stainless steel and the absence of voids in zirconium are in qualitative agreement with the formation energies for these extended defects according to Fig. 7.54.

Since we have just shown that the void is a stable configuration only for small numbers of vacancies, how then can we observe large voids with the number of vacancies exceeding several orders of magnitude? It is well established that for most metals, irradiation at low temperatures ($<0.2T/T_m$) results in aggregation of vacancies and interstitials to form clusters that are bound by dislocations, i.e., loops

Fig. 7.54 Formation energy
for various vacancy cluster
defects in (**a**) 316 stainless
steel and (**b**) zirconium as a
function of the log of the
number of vacancies in the
cluster. Material parameters
for stainless steel are
$\gamma_{SFE} = 35$ mJ/m^2,
$\gamma = 1.75$ J/m^2, and
$\mu = 82$ GPa. Material
parameters for zirconium are
$\gamma_{SFE} = 102$ mJ/m^2,
$\gamma = 1.40$ J/m^2, and $\mu = 33$ GPa
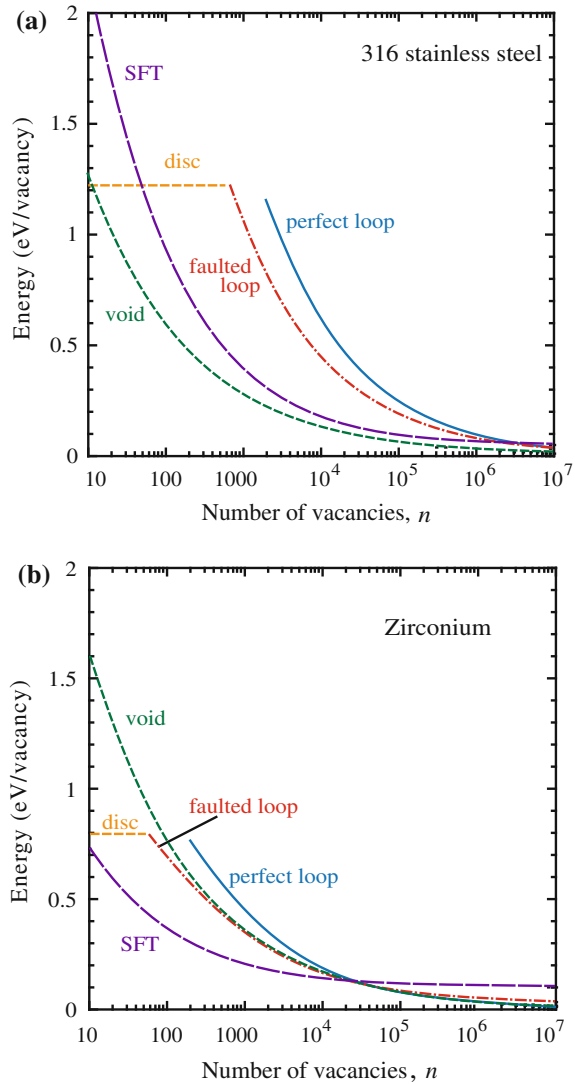
and SFT (in metals with low SFE). At higher temperatures, vacancies can also
aggregate to form voids. Voids appear in a band of temperatures ranging from about
$1/3 < T/T_m < 1/2$ where insoluble gases such as helium have a strong effect on
stabilizing voids. At temperatures less than $1/3T/T_m$, vacancies are not mobile
enough to reach the voids before annihilation with migrating interstitials. Also,
loops formed by vacancy collapse of cascades are stable against thermal dissoci-
ation at low temperatures and hence reduce the number of vacancies available for
void growth. At very high temperature, the thermal equilibrium vacancy concen-
tration becomes comparable with the radiation-induced vacancy concentration and

voids tend to shrink by vacancy emission. The subject of void and bubble nucleation and growth will be discussed in more detail in Chap. 8.

7.5   Effective Defect Production

With a better understanding the importance of defect clusters, we can expand and refine our description of defect production. Microstructure evolution is ultimately controlled by the migrating defect fractions of vacancies and interstitials, $MDF_{v,i}$. The most straightforward component of the MDF is the isolated point defect fraction, $IDF_{v,i}$ (discussed in Chap. 3), which is produced directly in the displacement cascade. A second component is the mobile cluster fraction, $MCF_{i,v}$ (discussed in Sect. 7.3.3) and is composed of mobile interstitial defect clusters and mobile vacancy clusters. The third component is defects released from clusters by evaporation, $EDF_{v,i}$, and is most important for vacancies and interstitials at very high temperatures. Taken together, these three sources of isolated defects comprise the migrating defect fraction, $MDF_{v,i}$. Zinkle and Singh [25] constructed a flow-chart to show the evolution of the various defect forms (Fig. 7.55), which is an expansion of the more simplistic case shown in Fig. 3.18 by inclusion of the processes in dashed boxes. Zinkle and Singh summarized experiments from which values for $MDF_{v,i}$ could be determined and found that in general $3\ \% < MDF_i < 10\ \%$ and $1\ \% < MDF_v < 10\ \%$ where the percentages refer to the calculated NRT production rate. While there is considerable uncertainty regarding the quantitative values deduced from experiments, the range can be used to bound the expected available defect fraction.

   The significance of these processes is that they are not often addressed in traditional rate theory models of microstructure evolution. To create an accurate physical model of defect production and accumulation under cascade damage conditions, the following must be included:

1. The production of a large fraction of defects heterogeneously in the form of vacancy and interstitial clusters with the remainder as isolated vacancies and interstitials
2. The bias for absorption of mobile interstitial clusters and freely migrating interstitials at sinks
3. The fractions of interstitials and vacancies in clustered or isolated forms that are not necessarily equal, which is equivalent to an asymmetric production of freely migrating fractions of vacancies and interstitials
4. Vacancy evaporation from clusters formed during the cascade quench that results in a temperature-dependent contribution to the fraction of freely migrating vacancies

As will be shown in subsequent sections and in the discussion of void formation and growth in Chap. 8, intracascade clustering and the thermal stability of interstitial and vacancy clusters cause an *asymmetry* in the supply of migrating

Fig. 7.55 Flowchart giving
the contributions to the
migrating defect fraction from
isolated defects, mobile defect
clusters, and evaporating
defects (after [25])

```
              ┌─────────────────────────────┐
              │ Displacement Cascade Efficiency │
              │            ( ξ )              │
              └─────────────────────────────┘
                            │
        ┌───────────────────┼───────────────────────────┐
        │                   │          ┌──────────────────┐│
        │                   └─────────▶│ Cascade Quench   ││
        │                              │ Annihilation And ││
        │                              │     Mixing       ││
        │                              └──────────────────┘│
        │      ┌─────────────────────────────┐            │
        │      │ Quenched Cascade Defect Fraction │        │
        │      │            (QDF)             │            │
        │      └─────────────────────────────┘            │
        └─────────────────────────────────────────────────┘
                            │
                            │        ┌──────────────────────┐
                            └───────▶│ Intracascade Thermal │
                                     │  Recombination ( ζ ) │
                                     └──────────────────────┘
                            │
              ┌─────────────────────────────┐
              │     Surviving Defect        │
              │  Fraction (SDF) ( ξ - ζ )   │
              └─────────────────────────────┘
```

Migrating Defect Fractions (MDF$_{i,v}$)

vacancies and interstitials, termed the *production bias* and this bias represents a
strong driving force for loop and void nucleation and growth.

7.6 Nucleation and Growth of Dislocation Loops

Dislocation loops resulting from vacancy and interstitial condensation are created
from clusters of the respective defects and either shrink or grow depending on the
flux of defects reaching the embryo. Once they have reached a critical size, the
loops become stable and grow until they unfault by interaction with other loops or
with the network dislocation density. The following sections describe the processes
of loop nucleation, growth, and unfaulting that determine the dislocation mi-
crostructure of a metal under irradiation.

Fig. 7.55 Flowchart giving
the contributions to the
migrating defect fraction from
isolated defects, mobile defect
clusters, and evaporating
defects (after [25])

Displacement Cascade Efficiency (ξ)

Cascade Quench Annihilation And Mixing

Quenched Cascade Defect Fraction (QDF)

Intracascade Thermal Recombination (ζ)

Surviving Defect Fraction (SDF) (ξ - ζ)

Clustered Point Defect Fraction (CDF) ($\delta_{i,v}$)

Isolated Point Defect Fraction (IDF) ($\gamma_{i,v}$)

Mobile Clusters

Immobile Clusters

Evaporating Defects

MCF$_{i,v}$ EDF$_{i,v}$ IDF$_{i,v}$

Migrating Defect Fractions (MDF$_{i,v}$)

vacancies and interstitials, termed the *production bias* and this bias represents a
strong driving force for loop and void nucleation and growth.

7.6 Nucleation and Growth of Dislocation Loops

Dislocation loops resulting from vacancy and interstitial condensation are created
from clusters of the respective defects and either shrink or grow depending on the
flux of defects reaching the embryo. Once they have reached a critical size, the
loops become stable and grow until they unfault by interaction with other loops or
with the network dislocation density. The following sections describe the processes
of loop nucleation, growth, and unfaulting that determine the dislocation mi-
crostructure of a metal under irradiation.

7.6.1   Loop Nucleation

Various attempts have been made to determine the nucleation rate of dislocation loops and voids. We will follow a treatment that is based on steady-state concentrations of vacancies and interstitials and assumes dilute solution thermodynamics, as developed by Russell et al. [26]. In this treatment, the effects of cascades are ignored. We will then introduce clustering theory and show how it can be applied to the loop nucleation problem to account for the formation of defect clusters in addition to point defects.

We begin by expressing the nucleation rate of a defect cluster of size n as the flux of clusters between adjacent size classes in a phase space of cluster size. Considering only one type of defect (vacancies, for example), the flux between any two adjacent size classes can be written as follows:

$$J_n = \beta_v(n)\rho(n) - \alpha_v(n+1)\rho(n+1), \tag{7.69}$$

where $\rho(n)$ and $\rho(n+1)$ are the numbers of n-mers (loops containing n vacancies) and $(n+1)$-mers per unit volume. $\beta_v(n)$ is the rate of vacancy capture by a n-mer, and $\alpha_v(n+1)$ is the rate of vacancy loss by a $(n+1)$-mer. The first term in Eq. (7.69) represents an addition to the $n+1$ size class by capture of a vacancy by a n-mer size class. The second term is a loss from the $(n+1)$-mer size class by emission of a vacancy. Figure 7.56 shows the various processes described by Eq. (7.69) in phase space. At steady state, $J_n = 0$ and Eq. (7.69) becomes the following:

$$\sigma_v(n+1) = \beta_v(n)\frac{\rho^0(n)}{\rho^0(n+1)}, \tag{7.70}$$

where $\rho^0(n)$ is the equilibrium concentration of n-mer vacancy loops. Substituting for $\alpha_v(n+1)$ from Eq. (7.69) into the expression for the nucleation rate, Eq. (7.70) yields the following:

$$\begin{aligned} J_n &= \beta_v(n)\left[\rho(n) - \rho(n+1)\frac{\rho^0(n)}{\rho^0(n+1)}\right] \\ &= -\beta_v(n)\rho^0(n)\left[\frac{\rho(n+1)}{\rho^0(n+1)} - \frac{\rho(n)}{\rho^0(n)}\right], \end{aligned} \tag{7.71}$$

and the term in brackets is just the derivative of the ratio $\rho(n)/\rho^0(n)$, or $\dfrac{\partial[\rho(n)/\rho^0(n)]}{\partial n}$. The nucleation rate then becomes:

$$J_n = -\beta_v(n)\rho^0(n)\frac{\partial[\rho(n)/\rho^0(n)]}{\partial n}, \tag{7.72}$$

capture

$\beta_v(n)$

n $\longrightarrow$ $n+1$

$\longleftarrow$

$\alpha_v(n+1)$

thermal emission
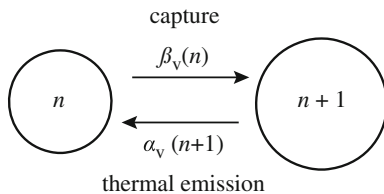
Fig. 7.56 Illustration of the capture and emission processes governing the flux of clusters between adjacent size classes in a phase space of cluster size

where

$$\rho^0(n) = N_0 \exp\left(-\Delta G_n^0/kT\right), \tag{7.73}$$

and N_0 is the number of nucleation sites per unit volume, and ΔG_n^0 is the free energy of forming the n-mer vacancy loop.

The steady-state nucleation rate of vacancy loops (consisting of k vacancies) can also be described as the product of the loop concentration, the jump frequency of the vacancy to the loop, and the jump distance, and is given by:

$$J_k = \rho_k^0 \beta_k Z, \tag{7.74}$$

where ρ_k^0 and β_k are the values of $\rho^0(n)$ and $\beta_v(n)$ at the critical size, k, and Z is the Zeldovich factor that depends on the curvature of ΔG_n^0 near the maximum, at the critical size. If ΔG_n^0 is approximated by a parabola in this region (lower curve in Fig. 7.57), then:

$$Z = \left[-\frac{1}{2\pi kT} \frac{\partial^2 \Delta G_n^0}{\partial n^2} \right]_{n_k}^{1/2}, \tag{7.75}$$

where the derivative is evaluated at the critical loop size, n_k. Its value is the width of ΔG_k^0 at kT units below the maximum and is on the order of 0.05.

Consider now the presence of interstitials in the vacancy loop nucleation formulation. The flux between any two size classes, say n and $n+1$, now becomes the following:

$$J_n = \beta_v(n)\rho(n) - \alpha_v(n+1)\rho(n+1) - \beta_i(n+1)\rho(n+1), \tag{7.76}$$

where all terms are as previously defined, and $\beta_i(n+1)$ is the rate of interstitial capture by a $(n+1)$-mer. Interstitial emission is of low probability and is neglected. Figure 7.58 shows the various processes described by Eq. (7.76) in phase space.

The rate of vacancy emission from a vacancy loop will be governed by temperature, size, and lattice energetics. Since the defect fractions are as high as 10^{-4}, a cluster has a defect in its immediate vicinity only this small fraction of time.
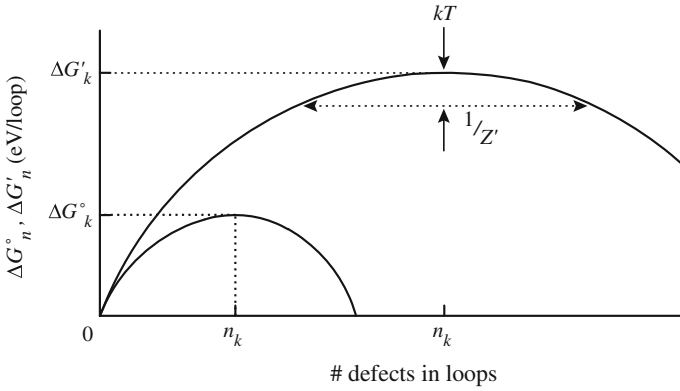
Fig. 7.57 Schematic nucleation curves showing the various parameters which are important in cluster nucleation. ΔG_k^0 is the activation barrier to nucleation if interstitials are not present, while $\Delta G_k'$ is the same quantity if interstitials are present during the vacancy cluster nucleation process (after [26])

The emission probability should be affected only slightly during this time interval and not at all otherwise. Therefore, we conclude that α_v is a value characteristic of a system without interstitials. Setting $J = 0$ in Eq. (7.76) is equivalent to equilibrating the size classes since there is no net flux between size classes. If we neglect interstitials, then from Eq. (7.76) we can write as follows:

$$\alpha_v(n+1) = \frac{\beta_v(n)\rho^0(n)}{\rho^0(n+1)}. \tag{7.77}$$

Combining Eqs. (7.76) and (7.77) gives:

$$J_n = \beta_v(n)\left\{\rho(n) - \rho(n+1)\left[\frac{\rho^0(n)}{\rho^0(n+1)} + \frac{\beta_i(n+1)}{\beta_v(n)}\right]\right\}. \tag{7.78}$$

Since $\rho^0(n) = N_0\exp(-\Delta G_n^0/kT)$, we note that:

$$\frac{\rho^0(n)}{\rho^0(n+1)} = \exp\left(\frac{\delta G_n^0}{kT}\right), \tag{7.79}$$
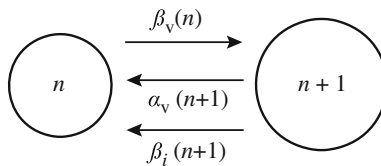
Fig. 7.58 Illustration of the capture and emission processes governing the flux of clusters between adjacent size classes in a phase space of cluster size and including the effect of interstitial capture

where $\delta G_n^0 \equiv \Delta G_{n+1}^0 - \Delta G_n^0$. The term δG_n^0 is the difference between the free energies of creating loops of $j + 1$ and j vacancies from single vacancies at the prevailing supersaturation. We now define new functions of n, $\rho'(n)$, and $\delta G_n'$ such that by analogy with Eq. (7.79):

$$\frac{\rho'(n)}{\rho'(n+1)} = \frac{\rho^0(n)}{\rho^0(n+1)} + \frac{\beta_i(n+1)}{\beta_i(n)} = \exp(\delta G_n'/kT), \tag{7.80}$$

where

$$\delta G_n' = \Delta G_{n+1}' - \Delta G_n', \tag{7.81}$$

and $\Delta G_n'$ is not generally a free energy because of the term $\dfrac{\beta_i(n+1)}{\beta_i(n)}$ in Eq. (7.80). Using the expression in Eq. (7.80), we can rewrite the equation for J_n in terms of $\dfrac{\rho'(n)}{\rho'(n+1)}$ by substituting Eqs. (7.80) into (7.78) to give the following:

$$J_n = \beta_v(n)\left\{ \rho(n) - \rho(n+1)\frac{\rho'(n)}{\rho'(n+1)} \right\}. \tag{7.82}$$

Rearranging Eq. (7.82) gives the following:

$$J_n = -\beta_v(n)\rho'(n)\frac{\rho(n+1)}{\rho'(n+1)} - \left[\frac{\rho(n)}{\rho'(n)}\right], \tag{7.83}$$

and noting that:

$$\frac{\left[\dfrac{\rho(n+1)}{\rho'(n+1)} - \dfrac{\rho(n)}{\rho'(n)}\right]}{\Delta n} = \frac{\partial\left(\dfrac{\rho(n)}{\rho'(n)}\right)}{\partial n}, \tag{7.84}$$

gives:

$$J_n = -\beta_v(n)\rho'(n)\frac{\partial[\rho(n)/\rho'(n)]}{\partial n}, \tag{7.85}$$

which is the basic flux equation. Rearranging Eq. (7.85) by taking the natural log of both sides and summing from $j = 0$ to $n - 1$ gives the following:

$$\sum_{j=0}^{n-1} \ln\left(\frac{\rho'(j)}{\rho'(j+1)}\right) = \sum_{j=0}^{n-1}\left\{ -\ln\left[\frac{\beta_i(j+1)}{\beta_v(j)} + \exp\left(\frac{\delta G_j^0}{kT}\right)\right] \right\}, \tag{7.86}$$

and

$$\ln\left(\frac{\rho'(n)}{\rho'(0)}\right) = \sum_{j=0}^{n-1}\left\{-\ln\left[\frac{\beta_i(j+1)}{\beta_v(j)} + \exp\left(\frac{\delta G_j^0}{kT}\right)\right]\right\}. \tag{7.87}$$

We can identify two boundary conditions. The first is the quantity $\rho'(0)$, which may be evaluated by noting that as $\beta_i(n)/\beta_v(n) \to 0, \rho'(0) = \rho^0(0)$ and that $\rho^0(0) \to N_0$, is simply the number of nucleation sites per unit volume. Since N_0 (and hence $\rho'(0)$) is independent of loop concentration, we can write the equation as follows:

$$\ln\left(\frac{\rho'(n)}{\rho'(0)}\right) = \sum_{j=0}^{n-1}\left\{-\ln\left[\frac{\beta_i(j+1)}{\beta_v(j)} + \exp\left(\frac{\delta G_j^0}{kT}\right)\right]\right\} = \frac{-\Delta G_n'}{kT}, \tag{7.88}$$

and

$$\Delta G_n' = kT\sum_{j=0}^{n-1}\ln\left[\frac{\beta_i(j+1)}{\beta_v(j)} + \exp\left(\frac{\delta G_j^0}{kT}\right)\right]. \tag{7.89}$$

Since $\beta_i(n)/\beta_v(n) \to 0, \rho'(0) \to \rho^0(0)$ and $\rho^0(0)$ is just N_0, the number of nucleation sites per unit volume, we have then:

$$\rho'(n) = N_0\exp\left(\frac{-\Delta G_n'}{kT}\right), \tag{7.90}$$

and

$$\Delta G_n^0 = \text{activation barrier without interstitials}$$
$$\Delta G_n' = \text{activation barrier with interstitials.}$$

The upper curve in Fig. 7.57 shows $\Delta G_n'$ as functions of n. Note that $\Delta G_n'$ is larger than ΔG_k^0 and requires a larger loop size due to the hindering effect of interstitials on the loop nucleation process. The maxima in the two curves occur at $n_k, \Delta G_k^0$ and n_k', $\Delta G_k'$.

Now, the steady-state loop nucleation rate may be calculated from the expression for J_n in Eq. (7.85):

$$J_k = Z'\beta_k\rho_k', \tag{7.91}$$

which is the rate at which loops escape over the potential barrier of height $\Delta G'_k$ in units of loops/cm^3 s. The term, β_k, is the rate of single vacancy impingement on a loop of size n'_k The term Z' is:

$$Z' = \left[-\frac{1}{2\pi kT} \frac{\partial^2 \Delta G'_n}{\partial n^2} \right]^{1/2}_{n'_k}. \tag{7.92}$$

The subscript indicates that the second derivative is to be evaluated at $n = n'_k$. As with Z in Eq. (7.75), its value is the width of $\Delta G'_k$ at kT units below the maximum and is of the order of 0.05. The second derivative is found from Eq. (7.69) to be:

$$\frac{1}{kT} \left(\frac{\partial^2 \Delta G'_n}{\partial n^2} \right)_{n'_k} = \left\{ \left[\frac{1}{kT} \frac{\partial^2 \Delta G^0_n}{\partial n^2} \right] \left[\exp\left(\frac{1}{kT} \frac{\partial \Delta G^0}{\partial n} \right) \right] \right\}_{n'_k}, \tag{7.93}$$

giving:

$$\rho'_k = N_0 \exp\left(-\Delta G'_k / kT \right), \tag{7.94}$$

where $\Delta G'_k$ is determined by evaluating Eq. (7.89) at n'_k.

The steady-state nucleation rate will not be established immediately after a sudden change in supersaturation or temperature, but will lag by a characteristic time, τ, known as the incubation time and is given by [26]:

$$\tau = 2(\beta_k Z'^2)^{-1}. \tag{7.95}$$

Equations (7.89) and (7.94) also apply for interstitial loop nucleation except that Z', $\beta_{k,}$ and ρ'_k are for interstitial loops rather than for vacancy loops, and $\Delta G'_n$ for interstitial loops is given as:

$$\Delta G'_n = kT \sum_{j=0}^{n-1} \ln\left[\frac{\beta_v(j+1)}{\beta_i(j)} + \exp\left(\frac{\delta G^0_j}{kT} \right) \right], \tag{7.96}$$

where δG^0_j is now the difference between the free energies of forming dislocation loops of $j+1$ and of j interstitials (in the absence of vacancies), β_k is the gross rate of interstitial capture by the loop of critical size, and $1/Z'$ is the width of $\Delta G'_n$ (for interstitials) a distance kT below the maximum at $\Delta G'_k$, and the net number of interstitials in the critical nucleus is denoted by n'_k. The critical loop size n'_k occurs at the maximum of $\Delta G'_n$ and is determined by solving $\partial \Delta G'_n / \partial n = 0$ for n'_k.

More recent treatments of the nucleation rate call for setting the all the fluxes in Eq. (7.69) equal to the steady-state flux, J_{ss}, leading to a family of equations [27]:

$$J_1 = \beta_v(1)\rho(1) - \alpha(2)\rho(2) = J_{ss} \tag{7.97}$$

$$J_2 = \beta_v(2)\rho(2) - \alpha(3)\rho(3) = J_{ss} \tag{7.98}$$

$$J_3 = \beta_v(3)\rho(3) - \alpha(4)\rho(4) = J_{ss} \tag{7.99}$$

$$\vdots$$

$$J_{n-1} = \beta_v(n-1)\rho(n-1) - \alpha(n)\rho(n), \tag{7.100}$$

where $n = n_v^{max}$. Letting the ratio of shrinkage to growth, $\alpha_k/\beta_v^k = r_k$ for all $k \le 2$, and letting $r_1 = 1$, the system of equations can be solved by multiplying the equations for J_k by the product of all the r_k with $k \le i$. That is, Eq. (7.98) is multiplied by r_2, Eq. (7.99) is multiplied by both r_2 and r_3. If the resulting set of equations is summed, all the r_k are eliminated except r_1 and r_n to yield:

$$J_1 = J_{SS} = \frac{\beta_v(1)\rho(1) - \alpha(n)\rho(n)\prod_{j=2}^{n-1} r_j}{1 + \sum_{k=2}^{n-1}\prod_{j=2}^{k} r_j}. \tag{7.101}$$

The product term in the numerator is eliminated by noting that (1) for a nucleation problem, the concentration of the monodefect, $\rho(1)$ will be much greater than $\rho(n)$, and (2) the ratio of the shrinkage to growth terms r_j is less than unity for $n > n_v^*$. Therefore, Eq. (7.101) becomes:

$$J_{SS} = \beta_v(1)\rho(1)\left[1 + \sum_{k=2}^{n-1}\prod_{j=2}^{k} r_j\right]^{-1}. \tag{7.102}$$

The advantage of this method to compute J_{ss} is the elimination of the Zeldovich factor and the approximations that must be made to compute it.

Russell [26] determined that based on vacancy and interstitial parameters and their likely supersaturations in a solid under irradiation, that interstitial loop nucleation is easier than vacancy loop nucleation because interstitial loop nucleation is much less sensitive to vacancy involvement than is vacancy loop nucleation to interstitial involvement. The primary reason is that S_i is expected to be several orders of magnitude greater than S_v during irradiation because of the very low equilibrium concentration of interstitials. Nevertheless, nucleation by this mechanism has been found to be difficult for both vacancy and interstitial loops, in contrast to the observation of stable loop growth after fairly low doses.

7.6.2   Clustering Theory

The nucleation of loops is essentially a clustering process in which enough of one type of defect needs to cluster, in the presence of the other type of defect, to result in a critical size embryo that will survive and grow. The cluster will shrink or grow depending on the net condensation rate of defects on clusters. Generalizing the description of cluster behavior in phase space given in the last section, and taking a vacancy loop as an example, vacancy clusters, v_j consisting of j vacancies will shrink or grow according to the following:

$$\begin{aligned}
\frac{\mathrm{d}v_j}{\mathrm{d}t} = K_{0j} &- \sum_{n-1}^{\infty}[\beta_{v_n}(j) + \beta_{i_n}(j)]v_j - \sum_{n=1}^{J}\alpha_{v_n}(j)v_j \\
&+ \sum_{n=1}^{j-1}\beta_{v_n}(j-n)v_{j-n} + \sum_{n=1}^{\infty}\beta_{i_n}(j-n)v_{j+n} \\
&+ \sum_{n=1}^{\infty}\alpha_{v_n}(j+n)v_{j+n} + \text{additional loss terms},
\end{aligned} \tag{7.103}$$

where β_{v_n} and β_{i_n} are the capture rates of migrating defect clusters v_n or i_n by a cluster of size v_j, and α_{v_n} is the corresponding emission or thermal dissolution rate. The first term on the RHS is the direct production of clusters of size j. The second term is the loss of clusters from size class j due to absorption of a vacancy or an interstitial cluster of size n, where $1 \le n < \infty$. The third term is the loss of clusters from size class j due to emission of vacancy clusters of size n. The fourth and fifth terms are the addition of clusters to size class j due to absorption of vacancy clusters by smaller size classes and the absorption of interstitial clusters by larger size classes. The sixth term is the addition of clusters to the size class j by loss of vacancy clusters from larger size classes and the "additional loss terms" allow for other mechanisms of contributing to the number of clusters in size class j.

Equation (7.103) can be solved numerically without further simplification. But for large clusters and long irradiation times, the number of equations required would be extremely large. A major simplification is to require clusters to grow or shrink by only the addition or loss of single point defects, resulting in:

$$\begin{aligned}
\frac{\mathrm{d}v_j(t)}{\mathrm{d}t} = K_{0j} &+ \beta(j-1,j)v_{j-1}(t) + \alpha(j+1,j)v_{j+1}(t) \\
&- [\beta(j,j+1) + \alpha(j,j-1)]v_j(t), \quad j \ge 2.
\end{aligned} \tag{7.104}$$

If it is assumed that j is a continuous variable and a Taylor series expansion is used in Eq. (7.104) to relate all functions to their values at size j, the simplified

description is a continuum diffusional approximation in size space, known as a *Fokker–Planck equation*:

$$\frac{\partial v_j(t)}{\partial t} = K_{0j}(t) - \frac{\partial}{\partial j}\left\{v_j(t)[\beta(j,j+1) - \alpha(j,j-1)]\right\}$$
$$+ \frac{1}{2}\frac{\partial^2}{\partial j^2}\left\{v_j(t)[\beta(j,j-1) + \alpha(j,j+1)]\right\}, \tag{7.105}$$

which is further simplified to:

$$\frac{\partial v_j(t)}{\partial t} = K_{0j}(t) - \frac{\partial}{\partial j}F_{v_j}v_j(t) + \frac{\partial^2}{\partial j^2}D_{v_j}v_j(t)$$
$$= K_{0j}(t) - \frac{\partial}{\partial j}\left(F_{v_j}v_j(t) - \frac{\partial}{\partial j}D_{v_j}v_j(t)\right). \tag{7.106}$$

The first term on the RHS of Eq. (7.106) is the direct production rate of clusters of size j. The second term is the *drift* in size space driven by the excess condensation of one point defect type over another:

$$F_{v_j} = (z_v D_v C_v - z_i D_i C_i) \tag{7.107}$$

The drift term is responsible for the shift of the cluster size distribution to larger sizes. The drift term ensures that a large cluster will inevitably grow in a radiation field, but due to the evolving microstructure, the drift contribution is not constant with dose. Cluster evolution is also very sensitive to the ratio of the concentration of vacancies and interstitials, as F_v contains the difference in their contribution and can change sign. The result is that the sign of F_v depends on the overall microstructure.

The third term is the *diffusion* in size space and D_{v_j} is the irradiation-enhanced diffusion coefficient given by:

$$D_{v_j} = \frac{1}{2}(z_v D_v C_v + z_i D_i C_i). \tag{7.108}$$

The diffusion term causes the cluster size distribution to broaden with dose. The diffusion term accounts for the fact that two different clusters introduced at the same time at the same size may differ in size at a later time due to random encounters with point defects.

Algorithms for the approximate solution of Eq. (7.106) are discussed by Golubov et al. [28]. The features of the Fokker–Planck equation are illustrated in Fig. 7.59 for the development of the interstitial loop size distribution for 316 stainless steel with initial dislocation density of 10^{13} m^{-2}, irradiated at 550 °C at a dose rate of 10^{-6} dpa/s. Note that with increasing dose, the mean loop size increases [drift term in Eq. (7.106)] and the size distribution broadens [diffusion term in Eq. (7.106)]. As small clusters grow and their geometry changes, so does the capture efficiency for freely migrating defects. For very large cluster sizes, the

Fig. 7.59 Development of
the interstitial loop size
distribution with dose in 316
stainless steel irradiated at a
dose rate of 10^{-6} dpa/s and a
temperature of 550 °C with
$\rho_d = 10^{13}$ m^{-2} (after [29])
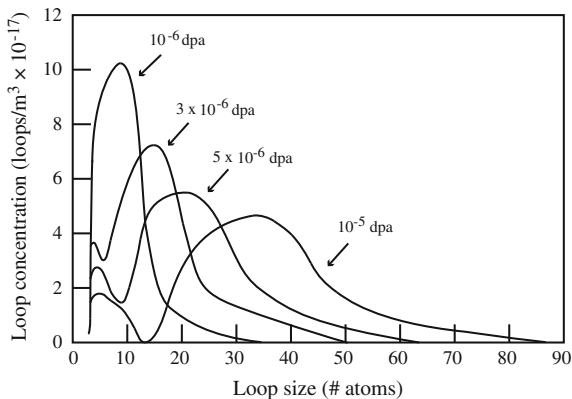
Fokker–Planck equation is too simple as the defect production and cluster growth
depend on the microstructure. The effect of the damage microstructure in the
evolution of defect clusters must be accounted for in order to accurately predict
their behavior.

7.6.3 Cluster Evolution Via Cluster Dynamics Modeling

The evolution of defect clusters can also be modeled using the cluster dynamics
method. Classical rate theory defines a defect cluster by its character, atomic
configuration, and size (or number of point defects contained within), but not by its
spatial position since the theory assumes that the concentration of each cluster is
homogeneous on a mean field basis. In cases such as shallow ion implantations,
very thin specimens, or bulk specimens with inhomogeneous microstructure, the
accurate treatment of spatially varying damage production or special effects such as
surface sinks and dislocation interaction necessitates the inclusion of spatial
dependence into rate theory-based models. One such spatially dependent cluster
dynamics code is PARASPACE, which incorporates one spatial dimension inten-
ded to account for situations where key physical variables depend on position in
one primary spatial direction.

As described by [30], PARASPACE treats clusters of intrinsic defects (either
self-interstitials or vacancies) and foreign gas atoms (helium, krypton). Since the
probability that self-interstitials (I) and vacancies (V) coexist in a single cluster is
very low due to their strong tendency for recombination, no mixed I–V clusters are
considered. Clusters are defined using just one number (subscript) i, with its
absolute value being the number of point defects (I or V) contained and its sign
("−" for I-clusters and "+" for V clusters) indicating the character of the cluster.
Two numbers, NI and NV, are chosen as the number of interstitials in the largest
I-cluster and the number of vacancies in the largest V cluster, respectively.

Physically, these numbers prescribe the "phase space" within which the clusters can interact with each other, and ensure the conservation of point defects. Numerically, these numbers, together with the number of spatial grids, NX, set the number of equations to be solved. NI and NV are chosen to be large enough so that the computation results are not affected by the prescribed phase space. Since the system may continuously evolve toward larger clusters, the initial values of NI and NV may become limiting at high dose. This is continuously checked within the PARASPACE code through the concentration and its gradient (with respect to i) at the phase boundaries. If certain thresholds are exceeded at the boundaries, the values for NI and NV are increased automatically and the time is reset to the last step prior to the occurrence of this event.

With 1D spatial dependence, the system of ordinary differential equations (ODE) describing defect evolution changes to a system of partial differential equations (PDEs), and the PDEs generally have the following generic form:

$$\frac{\partial C_i^{x_n}}{\partial t} = \phi \times P_i(x_n) + D_i \frac{\partial^2 C_i^{x_n}}{\partial x^2} + \text{GRT} + \text{GRE} + \text{ART} - \text{ARE}, \qquad (7.109)$$

where $C_i^{x_n}$ refers to the volumetric concentration (in nm^{-3}) of the ith cluster at the depth position x_n (in nm), ϕ is the particle flux (in $\text{nm}^{-2}\,\text{s}^{-1}$), $P_i(x_n)$ is the production "probability" (in $\text{particle}^{-1}\,\text{nm}^{-1}$) of the ith cluster by irradiation that is obtained through SRIM (combined with MD for intracascade recombination and clustering), D_i is the diffusivity of the ith cluster, GRT is the generation rate of the ith cluster by trapping reactions ($A + B \rightarrow i$) among other clusters, GRE is the generation rate of the ith cluster by emission processes ($C \rightarrow i + B$) of other clusters, ART is the annihilation rate of the ith cluster by its trapping reaction with other clusters ($i + B \rightarrow C$), and ARE is the annihilation rate of the ith cluster by its own emission process ($i \rightarrow A + B$).

The reaction terms differ slightly among different clusters, and the exact equation for the prescribed phase space ($\Lambda = [-\text{NI}, \text{NV}]$) is given as:

$$\frac{\partial C_i^{x_n}}{\partial t} = \phi \times P_i(x_n) + D_i \frac{\partial^2 C_i^{x_n}}{\partial x^2} + \sum_{\substack{m+p=i \\ m,p \neq 0 \\ m,p \in \Lambda}} k_{m,p}^{+} C_m^{x_n} C_p^{x_n} - \sum_{\substack{m \neq i \\ m \neq 0 \\ m,m+i \in \Lambda}} k_{m,i}^{+} C_m^{x_n} C_i^{x_n} - k_i^{-} C_i^{x_n},$$

$$(7.110)$$

for $i = \text{NV}$ or $-\text{NI}$, where k^{+} is the trapping reaction constant and k^{-} is the emission reaction constant.

Initially, vacancy and interstitial concentrations are set equal to their thermal equilibrium values and all cluster sizes are set to zero at all depth grids. The PDEs given in Eq. (7.110) are converted to ODEs by introducing the same set of clusters at each depth grid, and thus, the total number of ODEs is equal to the total number of clusters multiplied by the total number of depth grids. Then the diffusion terms in the PDEs are discretized as follows:

(a)

(b)
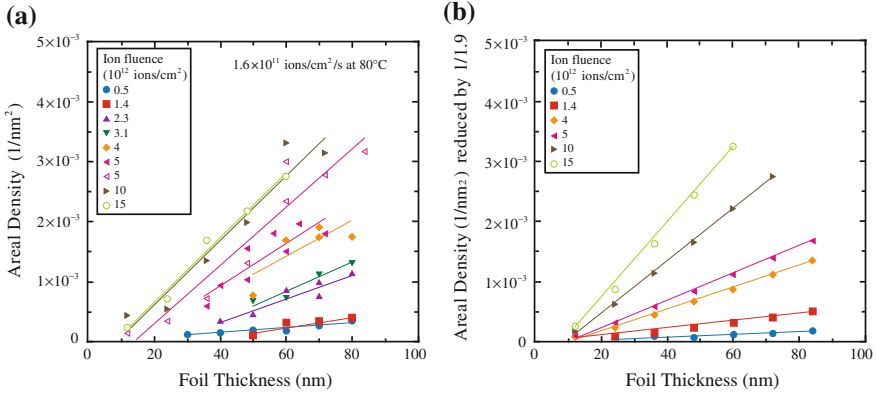
Fig. 7.60 Experimental (**a**) and model-predicted (**b**) areal densities of observable loops (diameter $\geq$ 1.3 nm) in Mo foils of various thicknesses irradiated at an ion flux of 1.6×10^{11} ions cm^{-2} s^{-1} at a temperature of 80 °C. The modeled densities were reduced by a factor of 1.9 to account for loops out of contrast in experiments (after [30])

$$D_i \frac{\partial^2 C_i^{x_n}}{\partial x^2} = D_i \frac{\dfrac{C_i^{x_n+1} - C_i^{x_n}}{x_{n+1} - x_n} - \dfrac{C_i^{x_n} - C_i^{x_n-1}}{x_n - x_{n-1}}}{\dfrac{(x_{n+1} - x_{n-1})}{2}}, \tag{7.111}$$

at all depth grids except the surface(s) where the black-sink boundary condition is enforced.

An example of the application of cluster dynamics modeling is irradiation of a thin foil of Mo with 1 MeV Kr$^+$ at a dose rate of 1.6×10^{11} ions cm^{-2} s^{-1} at a temperature of 80 °C. Figure 7.60 plots the areal density of observable loops (diameter $\geq$ 1.3 nm) observed experimentally (Fig. 7.60a) and modeled using the PASASPACE cluster dynamics code (Fig. 7.60b). Note that over a large range of doses, there is excellent qualitative agreement in the areal density of loops.

7.7   Dislocation Loop Growth

The growth of loops can also be determined from the Fokker–Planck equations that provide the size distribution of loops of all sizes (see Fig. 7.59). Applying Eq. (7.104) to the case of interstitial loops gives an equation in the form:

$$\frac{di_j}{dt} = K_{0j} + [\beta_v(j+1) + \alpha_i(j+1)]i_{j+1} - [\beta_v(j) + \beta_i(j) + \alpha_i(j)]i_j + \beta_i(j-1)i_{j-1}, \tag{7.112}$$

where i_j is the concentration of interstitial loops of size j and the term on the LHS of Eq. (7.112) is the time rate of change of the population of interstitial loops of size j. The terms $\beta_k(j)$ and $\alpha_k(j)$ are the absorption and emission rates of defects of type k from loops of size j. The first term on the RHS of the equality is the direct production rate of clusters of size j. Practically, this term is different from zero up to the tetrahedral cluster ($j = 4$). The first term in square brackets is the production of clusters of size j by the emission of an interstitial or absorption of a vacancy by clusters of size $j + 1$. The second term in square brackets is the loss of clusters of size j by absorption of a vacancy or an interstitial, or emission of an interstitial. The last term is the addition of clusters of size j by capture of an interstitials by clusters of size $j - 1$. Solution of Eq. (7.112) results in the loop size distribution as a function of time, which describes the evolution of interstitial loops with dose or time.

Pokor et al. [31] used the Fokker–Planck formalism to model the evolution of a population of loops via chemical rate theory in a homogeneous medium. In their treatment, they allowed for production of clusters in the cascade containing up to four defects and solved a set of equations for the concentration of defect clusters consisting of two equations for individual vacancies or interstitials and $2N$ equations for the population of loops up to size N. The physics of the formulation is contained in the expressions for the defect capture rates, β, and emission rates, α, for each defect type, k, as a function of the cluster size, given as [31]:

$$\beta_k(j) = 2\pi r(j) z_c(j) D_k C_k, \tag{7.113}$$

$$\alpha_k(j) = 2\pi r(j) z_c(j) \frac{D_k}{\Omega} \exp(-E_{bk}(j)/kT), \tag{7.114}$$

where $r(j)$ is the radius of an interstitial loop of size j, D_k and C_k are the diffusion coefficient and concentration of defect k, $z_c(j)$ is the bias factor for the interstitial loop of size j, and $E_{bk}(j)$ is the binding energy of for a cluster of j defects of type k. Pokor et al. [31] gives the following expressions for $z_c(j)$ and E_{bi}:

$$z_c(j) = z_i + \left(\sqrt{\frac{b}{8\pi a}} z_{li} - z_i \right) \frac{1}{j^{a_{li}/2}}, \tag{7.115}$$

$$E_b^i = E_f^i + \frac{E_b^{2i} - E_f^i}{2^{0.8} - 1} \left(j^{0.8} - (j-1)^{0.8} \right), \tag{7.116}$$

where z_i is the bias factor for a straight dislocation line for interstitials, a is the lattice parameter, and b is the Burgers vector, z_{li} and a_{li} are parameters used to describe the evolution of the bias with cluster size [32]. For the binding energy term, E_f^i is the formation energy of an interstitial point defect Eq. (4.16), E_b^{2i} is the binding energy of a two-interstitial cluster, and j is the number of defects in a cluster of size j and the expression comes from molecular dynamics simulations [33, 34].

To account for the effect of the annihilation of the network dislocation density with dose, they assumed that the rate of change of the density was proportional to $\rho^{3/2}$, giving $d\rho/dt = -Kb^2\rho^{3/2}$, and resulting in a dislocation density that decreases as $1/t^2$ (see next section). The network dislocation density in irradiated metals evolves toward a saturation value with increasing dose. In stainless steel, it has been observed to reach a saturation value of ~6×10^{-14} m^{-2} over a temperature range that spans 400–600 °C [35]. Cluster model results of the loop density and size for three grades of stainless steel irradiated at 330 °C and to doses up to 40 dpa calculated using Eqs. (7.112)–(7.116) are compared against measurements in Fig. 7.61 and show relatively good agreement. Dislocation recovery plays an important role in microstructure evolution as it represents a change in sink density. Failure to account for the recovery of the initial dislocation network would lead to a faster saturation of the loop structure in the 316 alloys. The most sensitive parameters controlling the irradiation microstructure are the temperature, dose, materials constants, and the initial network dislocation density.

Simpler treatments for determining the loop size distribution can be made by neglecting the formation of defect clusters larger than the tetra-interstitial, limiting the number of size classes and simplifying the cluster description. Stoller et al. [36] described the evolution of larger loops by the equation:

$$\frac{d\rho_j}{dt} = i_{j-1}\tau_j^{-1} - i_j\tau_{j+1}^{-1}, \tag{7.117}$$

Fig. 7.61 Evolution of the Frank loop (**a**) density and (**b**) size for 330 °C irradiation to high dose according to the cluster dynamics model of Pokor et al. (after [31])
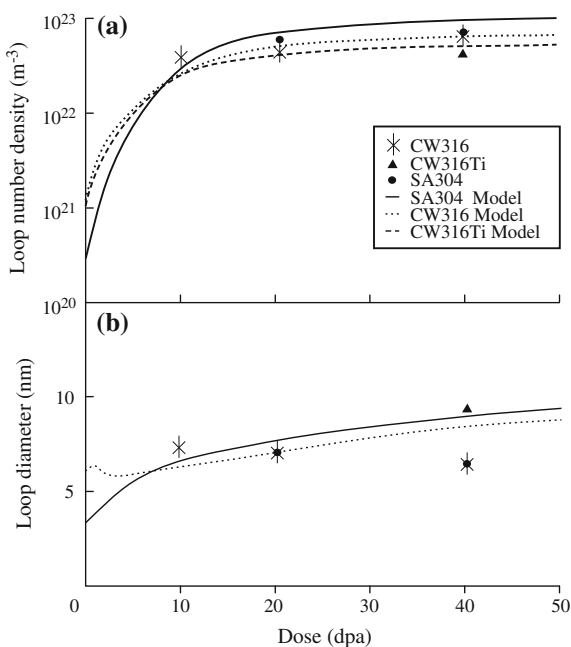
where ρ_j is the number of loops in a given size class with radius r_L, and the τ_j is the lifetime of a loop of size j against growth to the next larger size class:

$$\tau_j = \int_{r_j}^{r_{j+1}} \left(\frac{dr_L}{dt}\right)^{-1} dr_L, \tag{7.118}$$

and

$$\frac{dr_L}{dt} = \frac{\Omega}{b}[z_{iL}(r_L)D_iC_i - z_{vL}(r_L)D_v(C_v - C_{vL})], \tag{7.119}$$

where z_{iL} and z_{vL} are given by Eq. (5.100) and $C_{vL} = C_v^0 \exp(E_F\Omega/kT)$, and E_F is the energy of a faulted loop from Eq. (7.65). Figure 7.62a shows a comparison of the temperature dependence of the calculated maximum faulted loop density and low fluence fast reactor data for 316 stainless steel with initial network dislocation densities of 3×10^{15} m^{-2} (solid line) and 3×10^{13} m^{-2} (dashed line). Figure 7.62b shows the dose dependence of the loop density for solution annealed 316 irradiated at 500 °C.

Fig. 7.62 (a) Comparison of calculated maximum faulted loop density and low fluence fast reactor data as a function of temperature. (b) Dose dependence of faulted loop density for irradiation of solution annealed stainless steel at 500 °C (after [36])
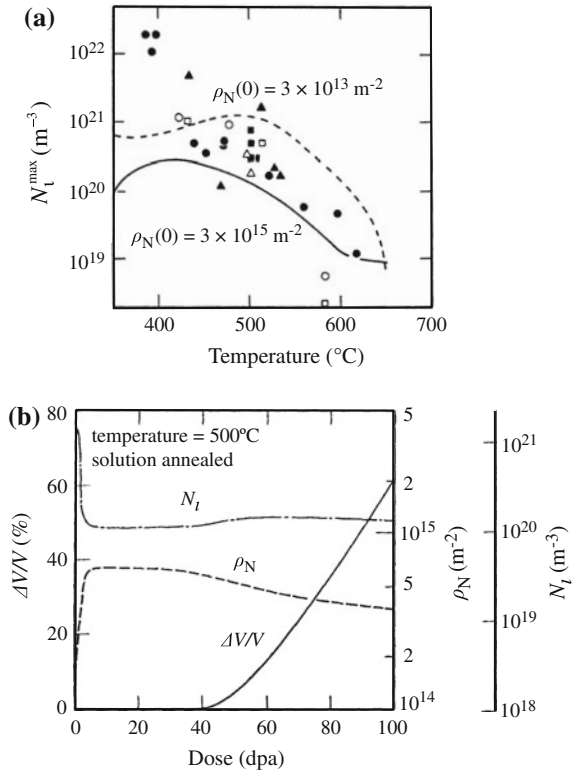
Semenov and Woo [37] accounted for the effect of production bias by writing Eq. (7.119) for the rate of change in loop size to include terms due to interstitial cluster and vacancy cluster absorption:

$$\frac{dr_L}{dt} = \frac{\Omega}{b} \left[J_i - J_v + J_v^e + J_i^{cl} - J_v^{cl} \right], \qquad (7.120)$$

where J_s are the fluxes due to single interstitials, single vacancies, vacancy thermal emission, interstitial clusters, and vacancy clusters, respectively, and τ_d is the lifetime of the dislocation loop. Substituting for the fluxes [36] results in:

$$\frac{dr_L}{dt} = \frac{K_0}{(\rho_N + \rho_L)b} \left(\frac{k_V^2 (\varepsilon_i - \varepsilon_v') + k_d^2 \bar{z}(1 - \varepsilon_i)}{k^2} - \frac{K^e}{K_0} \right), \qquad (7.121)$$

where K_0 is the defect production rate, K^e is the vacancy thermal emission rate, ρ_N and ρ_L are the network and loop dislocation densities, $\varepsilon_{i,v}$ is the fraction of interstitials and vacancies, respectively, that are immobilized by intracascade clustering, $\varepsilon_v' = \varepsilon_v - K^e/K_0$, z_d is the dislocation bias, $k_{V,d}^2$ are the sink strengths of voids and dislocations, k^2 is the total sink strength and $\bar{z} = \dfrac{z_d k_c^2}{k^2 + z_d k_d^2}$. The steady-state interstitial loop growth rate for 316 stainless steel with an effective point defect production rate of 10^{-7} dpa/s is shown as a function of temperature in Fig. 7.63. The growth rate is in units of Burgers vector, b per dpa. Note that the loop growth rate is low at low and high temperatures and peaks at an intermediate temperature of about 500 °C.

Fig. 7.63 Interstitial loop growth rate in units of Burgers vector, b per dpa as a function of temperature for a 316 stainless steel (after [38])
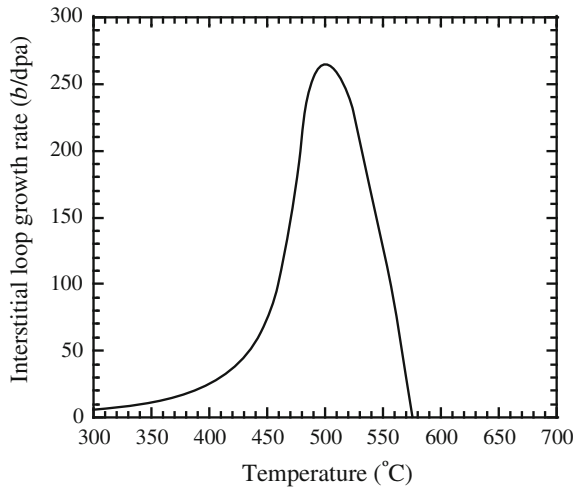
7.8 Recovery

Growing dislocation loops eventually encounter either network dislocations or each other. The maximum radius to which a loop can grow, R_{max}, is governed by the loop density, ρ_L as given by $\frac{4\pi}{3}\rho_L R_{max}^3 = 1$. When loops interact, they coalesce and contribute to the network dislocation density. Interaction between individual dislocations and loops results in loop unfaulting that also contributes to the network (discussed in Chap. 12, Sect. 12.3). As the dislocation density increases, the rate of loop interaction with the network increases and the loop radius is further limited by the network dislocation density as described by Eq. (5.85), $(\pi R_{max}^2)\rho_N = 1$.

However, observations of irradiated microstructures confirm that the dislocation density saturates, implying that there must also be a process for removal of network dislocations limiting their buildup. The process of recovery can explain the behavior of the dislocation density with irradiation. The rate of change of the dislocation density in a solid under stress at high temperature is assumed to behave according to:

$$\dot{\rho} = B\rho - A\rho^2, \tag{7.122}$$

where ρ is the density of mobile dislocations and A and B are constants [Note that while the rate of dislocation density change given by Eq. (7.122) is phenomenological by nature, a more accurate description of the physical process is provided by Eq. (7.117)]. The first term of Eq. (7.122) is the production rate of dislocations and the second term is the annihilation rate. The loss term is assumed to occur due to mutual annihilation of pairs of dislocations of opposite sign, which implies a reaction rate that is proportional to the square of the number of dislocations present at a given time. Garner and Wolfer [39] showed that the generation rate of dislocations is proportional to $b^2\phi\rho^{1/2}$, so that Eq. (7.122) can be written as:

$$\dot{\rho} = B\rho^{1/2} - A\rho^{3/2}, \tag{7.123}$$

where $B \sim b^2\phi$ and $A \sim v_c$, where v_c is the climb velocity of the dislocation (see Chap. 13). At steady state ($d\rho/dt = 0$), the saturation density is $\rho_s = B/A$. The solution to Eq. (7.122) is given as:

$$\frac{\rho(t)}{\rho_s} = \frac{1 - e^{-x} + \sqrt{\rho_0/\rho_s}(1 + e^{-x})}{1 + e^{-x}\sqrt{\rho_0/\rho_s}(1 - e^{-x})}, \tag{7.124}$$

where ρ_0 is the initial dislocation density and

$$x = A\sqrt{\rho_s}t = \sqrt{\rho_s}v_c t. \tag{7.125}$$

Fig. 7.64 (**a**) Calculated dislocation density evolution in 316 stainless steel at 500 °C using Eq. (7.139), for starting densities of 7×10^{15} m^{-2} and 4×10^{12} m^{-2}, for cold-worked and annealed conditions, respectively (after [34]). (**b**) Measured dislocation density in 20 % cold-worked and annealed 316SS after irradiation in EBR-II at 500 °C (after [40])
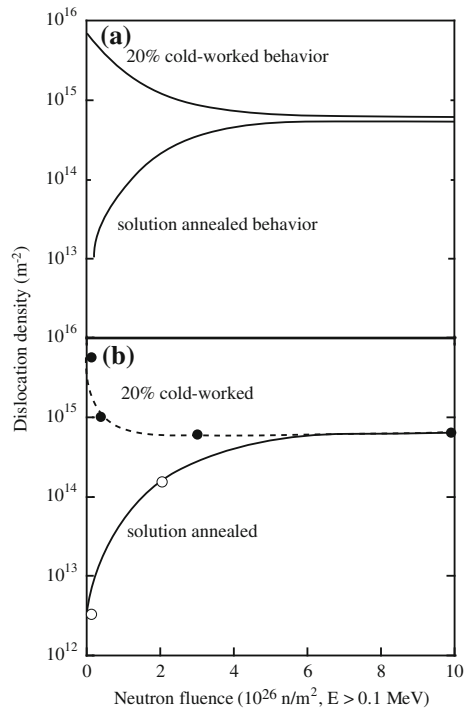
Using a saturation density, ρ_s of 6×10^{14} m^{-2}, and initial dislocation densities, ρ_0 of 3×10^{12} m^{-2} for annealed 316 SS and 7×10^{15} m^{-2} for 20 % CW 316 SS, the dislocation densities calculated from Eq. (7.123) are shown in Fig. 7.64a. The relationship between x in Eq. (7.124) and fluence was defined by the case where the dislocation density for annealed 316 SS reached a value of 2×10^{14} m^{-2} at 2×10^{26} n/m^2. Data are plotted in Fig. 7.64b. Note how well the model results of Fig. 7.64a agree with the data. This agreement also establishes that the original dislocations are not different from those produced during the irradiation with regard to their ability to absorb point defects.

7.9   Evolution of the Interstitial Loop Microstructure

The evolution of the interstitial loop population can be described in terms of its response to temperature and dose. The temperature regime that is important for LWR operation is between 270 and 340 °C. Higher temperatures may be reached from gamma heating in certain thick components such as PWR baffle plates. This temperature range represents a transition region between what is commonly termed as low-temperature (50–300 °C) and high-temperature (300–700 °C) behaviors.

Below 300 °C, the dislocation microstructure is characterized by a high density of "black dots" (defect clusters that are too small to resolve in the TEM, <2 nm), network dislocations, and a low density of Frank loops. A very small percentage of the small loops in stainless steels are observed to be SFT, which is much less than the 25–50 % of clusters in nickel or copper [10]. Near 300 °C, the radiation-induced microstructure changes from one dominated by small dislocation loops to one containing larger faulted loops and network dislocations (Fig. 7.65). Figure 7.66 shows large dislocation loops after irradiation at high temperatures. Above 300 °C, the Frank loop population begins to decrease. Figure 7.67 shows the sharp decrease in faulted loop density by a factor of over 1000 between 400 and 600 °C in neutron-irradiated austenitic stainless steels. The increase in loop size with temperature eventually leads to an increase in the loop unfaulting rate which contributes to the reduction in Frank loop population at high temperature.

Loop density increases rapidly to saturation at low irradiation temperatures. Figure 7.68 shows the increase in loop density in austenitic stainless steels irradiated near 300 °C. Loop size is relatively insensitive to fluence below about 300 °C. At these low temperatures, loop sizes and densities become dynamically stable as a population when a balance is reached between new loop formation and the destruction of existing loops. With increasing temperature in the low-temperature regime, the density of fine loops decreases and the loop size increases.

The dislocation microstructure evolves into one composed of Frank loops and network dislocations above about 300 °C. Loop density saturates at a few dpa and the density is maintained (in a dynamic sense) at higher doses. The dislocation network density increases in proportion to the faulted loop density as temperature is increased though the overall dislocation density is expected to stay fairly constant between 300 and 370 °C. In the higher temperature regime (400–600 °C), the population consists of a low density of Frank loops and a dislocation network.

Fig. 7.65 Effect of irradiation temperature in the range 50–400 °C on the components of the dislocation density in neutron-irradiated austenitic stainless steel (after [41])
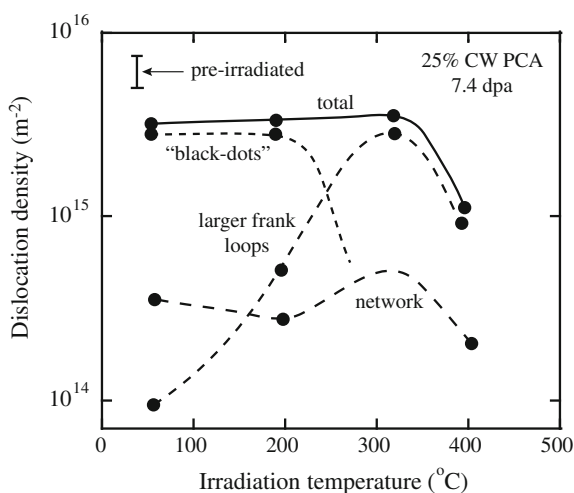
Fig. 7.66 Images of large
Frank loops in (**a**) a 300 series
stainless steel irradiated at
500 °C to a dose of 10 dpa
(from [42]), and (**b**)–(**e**) in
irradiated aluminum, copper,
nickel, and iron, respectively
(after [18])
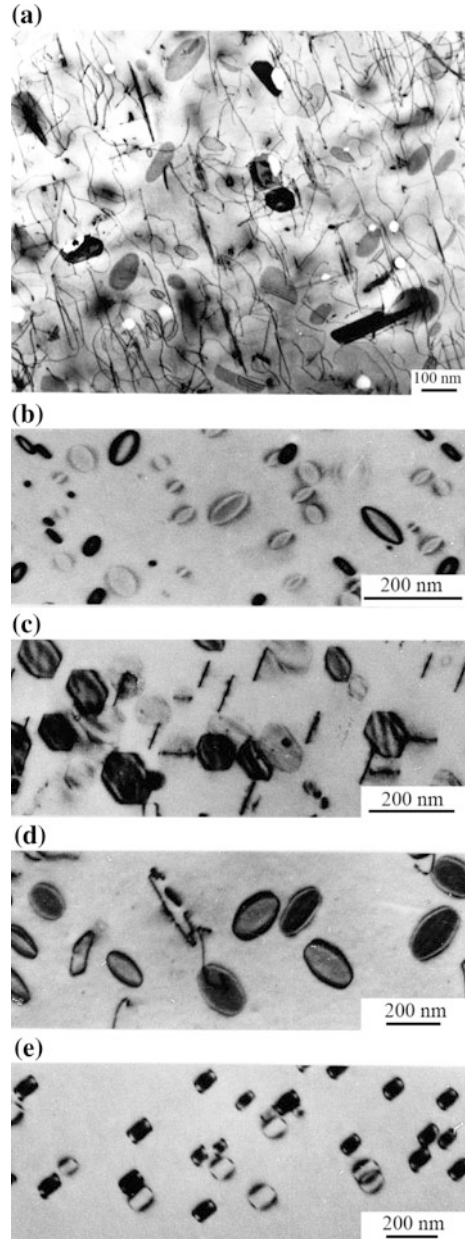
Evolution may actually occur more slowly if other microstructural processes are
also occurring such as void and bubble nucleation and growth.

The description of defect cluster nucleation and evolution provides a backdrop
for understanding the phenomenon of void growth discussed in the next chapter. As

Fig. 7.67 Effect of temperature on the Frank loop density in the intermediate temperature region, 400–600 °C, for neutron-irradiated austenitic stainless steel (after [41])
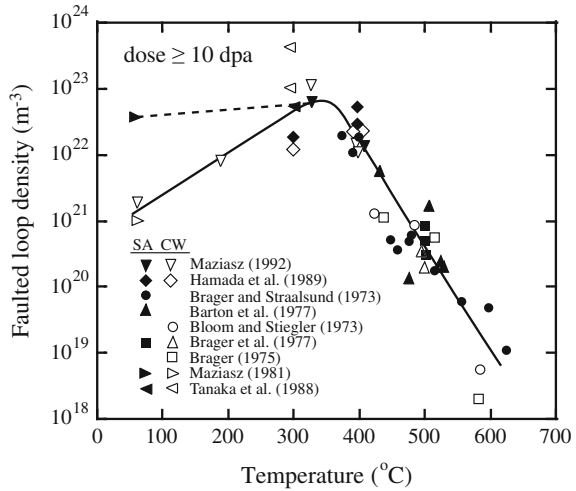
Fig. 7.68 Evolution of the Frank loop density and size in various austenitic stainless steels following irradiation to doses of up to 13 dpa at a temperature near 300 °C (after [43])
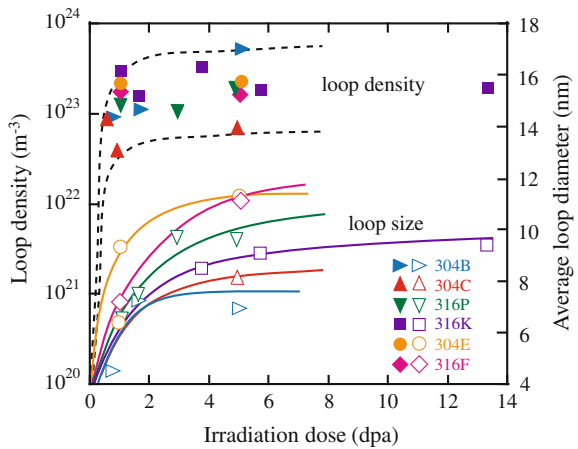
will be shown, void formation and growth is intimately linked to the production of defect clusters and their growth into loops, as these microstructures constitute critical sinks that will govern the fate of voids.

Nomenclature

a	Lattice constant
A	Area of slip plane
b	Burgers vector
$C_{v,i}$	Concentration of vacancies, interstitials
$C^0_{v,i}$	Thermal equilibrium concentration of vacancies, interstitials

d^x	Strength of diffusive spread for clusters by the x process
$D_{v,i}$	Diffusion coefficient of vacancies, interstitials
D_{k_j}	Diffusion term in size space of defect k and cluster size j, Eq. (7.106)
D_l	Climb diffusion coefficient
E	Energy
E_b	Binding energy
E_f	Formation energy
E_l	Dislocation loop energy
E_m	Migration energy
$\langle E_m \rangle$	Effective activation energy for cluster motion
f_i^{cl}	Fraction of interstitials in clusters
F_{k_j}	Drift velocity in size space of defect k and cluster size j Eq. (7.106)
G_j	Effective Frenkel pair production rate of species j
ΔG	Change in free energy
G_0	Standard free energy
i_n	Cluster of n interstitials
k	Boltzmann's constant
$k^{+/-}$	Rate constant for processes $+/-$ in cluster dynamics Eq. (7.110)
$k_{v,i}^2$	Total sink strength for vacancies, interstitials
l	Length of dislocation line segment
L	Length of edge of stacking fault tetrahedron
J	Nucleation current. Also flux
K_0	Defect production rate
K^e	Vacancy thermal emission rate
m	Stress exponent in relation between dislocation velocity and shear stress
$\boldsymbol{n}$	Unit vector
n_k, n_k'	Critical cluster size
N_d	Average number of defects generated in a single cascade
N_{il}	Number density of interstitial loop
N_0	Number of lattice sites per unit volume. Also number of nucleation sites
P_i	Probability of growing an interstitial cluster
P_m	Loop nucleation probability
r	Defect cluster radius
r_c	Dislocation core radius
r_L	Loop radius
r_k	Critical cluster radius
$\boldsymbol{s}$	Positive direction of the dislocation line
T	Temperature. Also PKA energy
$S_{v,i}$	Supersaturation of vacancies, interstitials
u_{ij}	Components of the displacement vector
v_g	Dislocation glide velocity
v_n	Cluster of n vacancies
V	Volume
W	Work

$z_{v,i}$	Vacancy, interstitial bias factor
Z	Zeldovich factor Eq. (7.75)
α_j	Emission rate of species j
β_j	Absorption rate of species j
γ	Shear strain. Also surface energy
γ_{SFE}	Stacking fault energy
δ	Thickness of void shell
ε_c	Strain associated with the dislocation core
ε_{ij}	Components of strain
ε_{i0}	Fraction of interstitials produced in cascades in the form of immobile clusters
Γ	Dislocation line tension
λ	Lamé constant
λ_d	Mean free path between consecutive interstitial cluster coalescing events
μ	Shear modulus
v	Poisson's ratio. Also jump frequency
$\rho(n)$	Number density of defect clusters of size n
v_s	Strength of drift term for clusters, by absorption of single defects
Ω	Atomic volume
ρ_x	Density of entity x
σ, σ_{ij}	Stress and components of stress
σ_s	Shear stress
σ_D	Value of shear stress that yields a dislocation velocity of 0.01 m/s
τ	Incubation time Eq. (7.95)
τ_d	Lifetime of dislocation loop

Subscripts

c	Dislocation core
d	Dislocation
i	Interstitial
k	Critical cluster size
L	Loop
F	Frank loop
N	Dislocation network
P	Perfect loop
v	Vacancy
0	Initial

Superscripts

c	Coalescence
cl	Clusters
s	Single defects

+   Trapping
−   Emission

Acronyms

ARE   Cluster annihilation rate by emission
ART   Cluster annihilation rate by trapping
EDF   Evaporating defect fraction
GRE   Cluster generation rate by emission
GRT   Cluster generation rate by trapping
IDF   Isolated point defect fraction
MCF   Mobile cluster fraction
MDF   Mobile defect fraction
NI   Largest interstitial cluster
NN   Nearest neighbor
NV   Largest vacancy cluster
PBM   Production bias model
PKA   Primary knock-on atom
SFE   Stacking fault energy
SIA   Single interstitial atom
UHP   Ultra-high purity

Problems

7.1. Draw billiard ball models of the extra half sheet of atoms which constitute the following dislocations:

   (a) The a/2[110] edge dislocation in the (111) plane of the fcc lattice.
   (b) The a/2[111] edge dislocation on the (110) plane of the bcc lattice.

7.2. It is found experimentally that a certain material does not change in volume when subjected to an elastic state of stress. What is Poisson's ratio for this material?

7.3. Determine the volume of a 10 cm diameter copper sphere that is subjected to a fluid pressure of 12 MPa.

7.4. Assuming that atoms are hard elastic spheres, show that Poisson's ratio for a close-packed array of spheres is 1/3.

7.5. For a circular shaped disk lying on the (111) plane of an fcc crystal:

   (a) Determine the energy as a function of the number of vacancies.
   (b) How many vacancies could a spherical void have before it would spontaneously convert to a vacancy disc?

7.6. It is known that the amount of stored energy in a solid can be increased with the addition of dislocations.

   (a) Calculate this energy for aluminum with a dislocation density of 10^{12} m^{-2}.
   (b) It has also been suggested that this energy can be increased by application of a shear stress, σ_s. Given that the straight edge dislocations in part (a) are in the form of an equally spaced cubic-shaped network, determine the shear stress, σ_s, needed to bow each dislocation segment into a half circle, and calculate the resulting increase in stored energy.

7.7. Calculate the net density of edge dislocations in a thin simple cubic crystal with lattice parameter $a = 2 \times 10^{-8}$ cm if it is bent to have a radius of curvature of 10 cm. (The thickness of the crystal is no greater than 1 mm.)

7.8. In the circular shear loop shown in the figure below, let the x-axis be the direction of the Burgers vector shown in the drawing, the z-axis in the plane of the loop but perpendicular to the direction of the Burgers vector, and the y-axis perpendicular to the plane of the loop. Let θ be the polar angle of the circle measured from point A. At any point θ on the loop, the Burgers vector has an edge component b_e that is perpendicular to the dislocation line at that position and a screw component b_s that is parallel to the line.

   (a) Using the fact that the vector $\boldsymbol{b}$ with these components is constant (in magnitude and direction) at all points on the loop, derive expressions for b_e and b_s as functions of θ.
   (b) Suppose a shear stress σ_{xy} is applied to the loop. Show that the resultant force on the dislocation line is always radially directed and has a magnitude $\sigma_{xy}b$.
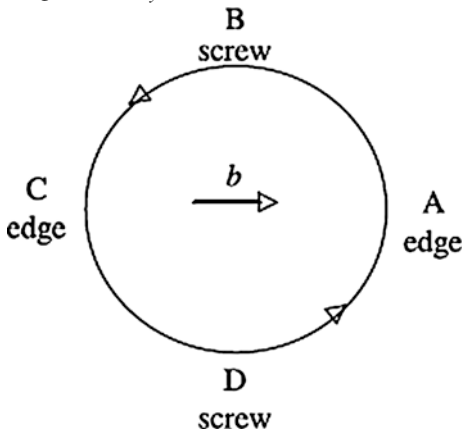
7.9. Plot the stress fields surrounding edge and screw dislocations as a function of θ. Specifically, plot the following:

   (a) σ_{xx}, σ_{yy}, and σ_{xy} versus θ for an edge dislocation
   (b) σ_{xz} and σ_{yz} versus θ for a screw dislocation

7.10. For the dislocations in the figure below:

(a) Calculate the magnitude of the components of force on dislocation
    (2) due to dislocation (1).
(b) Repeat part (a) for angles of 0°, 30°, 45°, and 90°.
(c) At $\theta = 30°$, will dislocation (2)

  (i) glide toward or away from dislocation (1)?
  (ii) tend to climb up or down? Why?
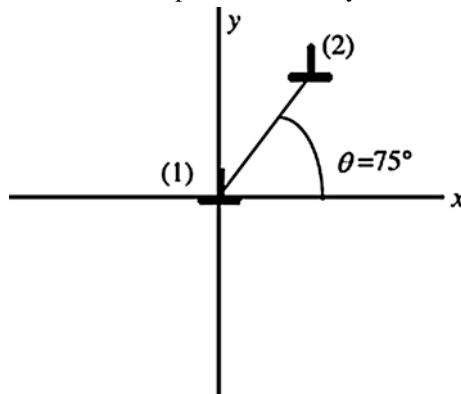
7.11. For the dislocations given in the sketch, find

(a) The force on dislocation (2) due to dislocation (1)
(b) In which direction will dislocation (2) climb and/or glide?
(c) Describe the stress and temperature dependence of these two processes
    and under what circumstances each will contribute to creep.
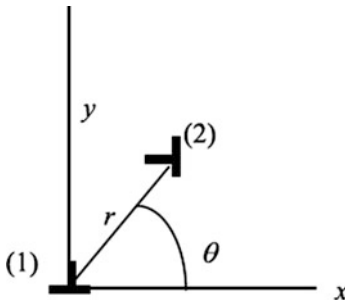
(1) $s = |001|, b = b|100|$
(2) $s = |00\bar{1}|, b = b|0\bar{1}0|$

7.12. An edge dislocation having the properties $s = k$ and $b = bj$ is on a plane
    $x = X$. Calculate the y-coordinates of the maxima and minima of the glide and

climb forces (separately) that it would experience due to a fixed dislocation at the origin ($s = k$) for the following three cases:

(a) $b = bi$
(b) $b = bj$
(c) $b = b(1/2i + \sqrt{3}/2j)$.

7.13. An edge dislocation (1) with $s = [001]$ and $b = b[100]$ is located at the origin of a coordinate system. Another edge dislocation (2) with $s = [001]$ and $b = b[\sqrt{2}\sqrt{2}0]$ is located a distance r away from (1) and 45° CCW from the x-axis.

(a) Calculate the glide and climb force on dislocation (2) due to dislocation (1).
(b) Make a graph of the force on dislocation (2) as a function of θ (for a given r) for $0 \leq \theta \leq 2\pi$.

7.14. Compute the local force on dislocation (2) due to dislocation (1) for the four examples of interaction between two perpendicular dislocations listed below:

$$s_1 = [001] \qquad s_2 = [010]$$

$$b_1 = b \begin{cases} [100] \\ [100] \\ [100] \\ [010] \end{cases} \quad b_2 = b \begin{cases} [100] \\ [010] \\ [001] \\ [010] \end{cases}$$

where the first dislocation passes through $x = y = 0$ and is parallel to the z-axis, and the second dislocation passes through $x = X$ and $z = 0$ and is parallel to the y-axis.

(a) In which cases does the total force on dislocation (2) vanish?
(b) If dislocation is able to flex, sketch the shape it is likely to assume provided the first dislocation passing through $x = 0$ remains straight.

References

1. Weertman J, Weertman J (1964) Elementary dislocation theory. Macmillian, London
2. Hull D, Bacon DJ (1984) Introduction to dislocations. Pergamon, Oxford
3. Friedel J (1964) Dislocations. Pergamon, New York
4. Hirth JP, Lothe J (1982) Dislocations in crystals, 2nd edn. Wiley Interscience, New York
5. Reed-Hill RE, Abbaschian R (1994) Physical metallurgy principles, 4th edn. PWS, Boston
6. Hull D, Bacon DJ (2001) Introduction to dislocations, 4th edn. Butterworth Heinemann, Philadelphia
7. Dieter GE (1976) Mechanical metallurgy, 2nd edn. McGraw-Hill, New York, p 180
8. Osetsky YN, Stoller RE, Matsukawa Y (2004) J Nucl Mater 329–333:1228–1232
9. Bacon DJ, Osetsky YN, Stoller RE, Voskoboinikov RE (2003) J Nucl Mater 323:152–162
10. Bacon DJ, Gao F, Osetsky YN (2000) J Nucl Mater 276:1–12

11. Stoller RE (2012) Primary radiation damage formation. In: Konings RJM (ed) Comprehensive nuclear materials. Elsevier, Amsterdam, p 293
12. Phythian WJ, Stoller RE, Foreman AJE, Calder AF, Bacon DJ (1995) J Nucl Mater 223:245–261
13. Osetsky YN, Bacon DJ, Serra A, Singh BN, Golubov SI (2000) J Nucl Mater 276:65–77
14. Gao F, Bacon DJ, Flewitt PEJ, Lewis TA (1997) J Nucl Mater 249:77–86
15. Valo M, Krause R, Saarinen K, Hautojarvi P, Hawthorne JR (1992) In: Stoller RE, Kumar AS, Gelles DS (eds) Effects of radiation on materials, ASTM STP, vol 1125. American Society for Testing and Materials, West Conshohocken, pp 172–185
16. Stoller RE (2000) J Nucl Mater 276:22–32
17. Jenkins ML, Kirk MA (2001) Characterization of radiation damage by transmission electron microscopy. Institute of Physics, Philadelphia
18. Kiritani M (1994) J Nucl Mater 216:200–264
19. Osetsky YN, Sera A, Singh BN, Golubov SI (2000) Philos Mag A 80:2131
20. Heinisch HL, Singh BN, Golubov SI (2000) J Nucl Mater 283–287:737
21. Wirth BD, Odette GR, Marondas D, Lucas GE (2000) J Nucl Mater 276:33–40
22. Johnson RA (1967) Phil Mag 16(141):553
23. Jossang T, Hirth JP (1966) Phil Mag 13:657
24. Kelly BT (1966) Irradiation damage to solids. Pergamon, New York
25. Zinkle SJ, Singh BN (1993) J Nucl Mater 199:173–191
26. Russell KC, Powell RW (1973) Acta Meta 21:187
27. Stoller RE, Odette GR (1987) In: Gerner FA, Packan NH, Kumar AS (eds) Radiation-induced changes in microstructure: 13th international symposium (Part I), ASTM STP 955. American Society for Testing and Materials, Philadelphia, pp 358–370
28. Golubov SI, Ovcharenko AM, Barashev AV, Singh BN (2001) Phil Mag A 81(3):643–658
29. Ghoniem NM, Sharafat S (1980) J Nucl Mater 92:121–135
30. Xu D, Wirth BD, Li M, Kirk MA (2012) Acta Mater 60:4286–4302
31. Pokor C, Brecht Y, Dubuisson P, Massoud JP, Barbu A (2004) J Nucl Mater 326:19–29
32. Duparc AH, Moingeon C, Smetniansky-de-Grande N, Barbu A (2002) J Nucl Mater 302:143
33. Soneda N, Diaz de la Rubia T (1998) Phil Mag A 78(5):995
34. Osetsky YN, Serra A, Victoria M, Golubov SI, Priego V (1999) Phil Mag A 79(9):2285
35. Garner FA, Kumar AS (1987) Radiation-induced changes in microstructure: 13th international symposium (Part I), ASTM STP 955. American Society for Testing and Materials, Philadelphia, pp 289–314
36. Stoller RE, Odette GR (1987) In: Garner FA, Packan NH, Kumar AS (eds) Radiation-induced changes in microstructure: 13th international symposium (Part I), ASTM STP 955. American Society for Testing and Materials, Philadelphia, p 371
37. Semenov AA, Woo CH (2003) Phil Mag 813:3765–3782
38. Eyre BL, Bullough R (1965) Phil Mag 12:31
39. Garner FA, Wolfer WG (1982) In: Brager HR, Perrin JS (eds) Effects of radiation on materials: 11th conference, ASTM STP 782. American Society for Testing and Materials, West Conshohocken, p 1073
40. Garner FA (1994) In: Frost BRT (ed) Materials science and technology (chapter 6), vol 10A. VCH, New York, p 419
41. Zinkle SJ, Maziasz PJ, Stoller RE (1993) J Nucl Mater 206:266–286
42. Mansur LK (1994) J Nucl Mater 216:97–123
43. Edwards DJ, Simonen EP, Bruemmer SM (2003) J Nucl Mater 317:13–31